Self-Assembly of Nanoalloys

Harald Brune, Alexa Courty, Christophe Petit, Vincent Repain

▶ **To cite this version:**

Harald Brune, Alexa Courty, Christophe Petit, Vincent Repain. Self-Assembly of Nanoalloys. Florent Calvo. Nanoalloys. From fundamentals to emergent applications - Second edition, Elsevier, pp.451-487, 2020, 978-0-12-819847-6. 10.1016/B978-0-12-819847-6.00018-8 . hal-03943880

HAL Id: hal-03943880

https://cnrs.hal.science/hal-03943880v1

Submitted on 17 Jan 2023

HAL is a multi-disciplinary open access archive for the deposit and dissemination of scientific research documents, whether they are published or not. The documents may come from teaching and research institutions in France or abroad, or from public or private research centers.

L'archive ouverte pluridisciplinaire **HAL**, est destinée au dépôt et à la diffusion de documents scientifiques de niveau recherche, publiés ou non, émanant des établissements d'enseignement et de recherche français ou étrangers, des laboratoires publics ou privés.

Self-assembly of nanoalloys

H. Brune[1], A. Courty[2], C. Petit[2] and V. Repain[3]

[1] Ecole Polytechnique Fédérale de Lausanne (EPFL), Insitute of Condensed Matter Physics (ICMP), Station 3, CH-1015 Lausanne, Switzerland
E-mail : harald.brune@epfl.ch

[2] Sorbonne Université, CNRS, MONARIS, UMR 8233, 4 place Jussieu, 75005 Paris (France), 4 place Jussieu, F-75005, Paris, France
E-mail : christophe.petit@sorbonne-universite.fr

[3] Laboratoire Matériaux et Phénomènes Quantiques (UMR 7162), Bâtiment Condorcet, Case courrier 7021, Université Paris Diderot-Paris 7, CNRS, 75205 Paris cedex 13, France
E-mail : vincent.repain@univ-paris-diderot.fr

In this chapter, we focus on the use of inorganic nanocrystals (nanoalloys or homogeneous) as building blocks to elaborate a new class of materials with unique properties compared to the single nanoparticles or solid materials. Chemical and physical approach of the self-organization are then presented and discussed.

List of abbreviations

TEM: Transmission electron microscopy
SEM: Scanning electron microscopy
SEM-FEG: Scanning electron microscopy- field emission gun
SAXRD: Small angle X-ray diffraction
NC: nanocrystals
HOPG: Highly oriented pyrolitic graphite
Superlattices or super-crystals: periodic organization of nano-objects
BNSL: binary superlattices madefrom two differents nano-objects

11.1 Introduction

A key issue in the realization of nanoparticles is the narrowing of the size distribution. Most applications in catalysis, magnetic recording, etc. require monodisperse particles. From a fundamental point of view, it is also of great interest for the understanding of chemical and physical properties by means of averaging techniques to work with monodisperse samples. Furthermore, the organization of particles into arrays can lead to new controlled collective properties that are exacerbed if the particles are monodisperse. Furthermore, and as the main focus of this entire book, there is a great interest for the development of new materials based on bimetallic nanoparticles, which can lead to potential applications in various areas. These include advanced optical (Chapter 7) or magnetic (Chapter 8) nano-devices, catalysis (Chapter 9) or biological imaging (Chapter 10). In the past years, a number of different routes have been developed in order to achieve arrays of nanostructured alloys that we review in this chapter. We mainly focus on self-assembly techniques, either chemical or physical in nature, which can form impressively dense 2D or 3D arrays of nanometer-size bimetallic nanoparticles or binary superlattices made of different monometallic nanoparticles. We explain the principles of ordering and the key parameters driving the quality of the arrays. We illustrate the different methods by a selection of examples of bimetallic systems, either mixed or in core-shell geometry.

11.2 Chemical routes

Monodisperse inorganic nanocrystals (NCs) coated by organic ligands are the building block of 2D and 3D super-organizations. It should be mentioned that nanoalloys considered as building block, do not present specificity due to their composition: assemblies of NCs are stabilized by van der Waals interactions, the interactions, bonding within the super-crystals resulting from the interdigitation of the ligand molecules. From a chemical point of view, the crystallization of 2D or 3D superlattices is a thermodynamically driven process, which depends on both the homogeneity of the NC building blocks and on the self-assembly conditions.
The main strategies for the chemical route for self-assembly of NCs involve either: i) interfacial self-assembly (liquid-gas, liquid-liquid or liquid-solid); ii) processes in solution; iii) template of external forces (directed self-organization). We will focus here on the two first strategies, the third one being more representative of the physical route and will be expanded in section 11-3. As a general rule, self-organization of NCs requires a low size and reduced shape polydispersity [1]. The elaboration of 2D and 3D superlattices is generally performed by controlled evaporation of the organic solvent from a suspension of monodisperse NCs deposited on a solid

substrate [2]. A large variety of 2D and 3D ordered structures have been obtained in this way [3-10].

11.2.1 2D self-assembly of inorganic nanocrystals

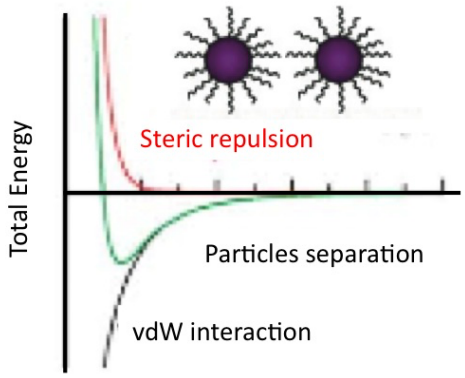

Fig. 11.1. Typical energy curves describing the nanoparticles stability in apolar solvent (from Ref 11), reproduced with permission.

Besides the narrow size and shape distribution, the self-organization phenomenon is strongly influenced by inter-particle forces but also by the interaction between the substrate and the NCs, which can be mediated by the capping agent (the organic ligand, which is always present in the chemical process to stabilize the NCs) and by the solvent used to disperse the NCs [11]. In apolar solvents (mainly used in chemical self-assembly processes) and for nearly spherical NCs, the inter-particle forces in a colloidal solution mainly act in an isotropic way. The attractive energy results from the attractive forces (E_{vdW}) between the metal cores while the repulsive energy results from the steric repulsive forces (E_s) between the ligand shells (Figure 11.1). In a simple model, and in case of hydrophobic dodecylthiol-capped silver NCs, Korgel et al. expresszs E_{vdW} and E_s as follows [12]:

(1) $$E_s = \frac{100Rl^2}{(d-2R)\pi\sigma_l^3} kT \exp\left(\frac{-\pi(d-2R)}{l}\right)$$

$$E_{vdW} = -\frac{A}{12}\left\{\frac{4R^2}{d^2-4R^2} + \frac{4R^2}{d^2} + 2Ln\left[\frac{d^2-4R^2}{d^2}\right]\right\} \qquad (2)$$

where d is the interparticle distance (center to center), $2R$ the diameter of the particles, l the length of the capping agent and σ_l its surface per polar head group. A is the so-called Hammaker constant taking into account the nature of the material and k the Boltzmann constant. It should be noticed that it is a simplified picture of the true interactions. The interaction with the substrate during the deposition process

[13], the nature of the solvent (good or bad solvent of the capping agent) [14,15] and the attractive interaction between the capping molecules (interdigitation or bundling) [16] could also play important roles in the self-assembly process (see below).

11.2.1.1- Role of the substrate on the 2D assemblies made of inorganic nanocrystals

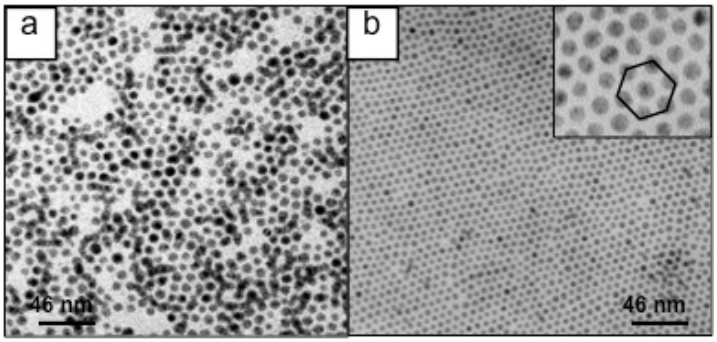

Fig. 11.2. Transmission electron microscopy (TEM) image of silver NCs deposited on a) amorphous carbon; b) on HOPG in insert (TEM) pattern at higher resolution showing that the NCs are organized in a hexagonal network.

The 2D self-organized film made of inorganic NCs can be obtained by direct deposition of drops of nanocrystals solution on a solid substrate or carbon coated TEM grid. In some case, controlled evaporation could also be used [17].

Influence of the roughness of the substrates

Figure 11.2 shows images of the same dodecylthiol-capped silver NCs deposited on TEM grids coated either by amorphous carbon (Fig. 11.2A) or by thin sheets of HOPG (Fig. 11.2.B). Silver nanoparticles were synthesized via reverse micelles techniques and are characterized by a low size distribution (around 11%) [17]. Films were obtained by depositing drops of a NCs solution on the transmission electron microscopy (TEM) grid with a filter paper underneath. Using amorphous carbon as a substrate, the ordering is local and the monolayers show vacancies (Fig. 11.2A). 2D organization of the same silver nanoparticles is improved on HOPG characterized by a low roughness, which favors the nanoparticle diffusion and thus their organization (Fig 11.2B). The organization acts over a long range in a hexagonal network (see inset). The interparticle spacing is found to be around 2 nm, less than twice the thickness of a dodecylthiol self-assembled monolayer on a flat surface. This suggests some interdigitation of chains between neighboring particles. A siimilar effect has been obtained with different materials including gold [11,18], cobalt [19], platinum [20] or nanoalloys such as FePt [21,22] and CoPt [23,24].

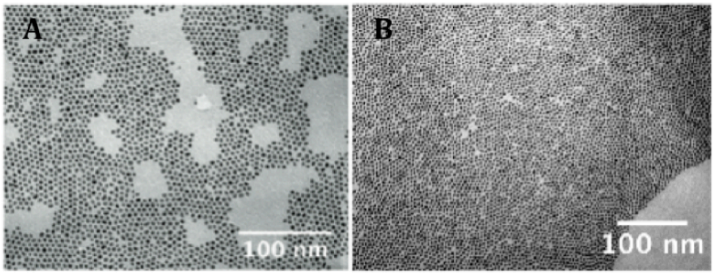

Fig. 11.3. 2nm CoPt nanoalloys deposited on TEM grid coated with (A) amorphous carbon; (B) thin sheets of HOPG. The compactness of the monolayers increases depending on the wettability of the substrate.

Figure 11.3 shows TEM patterns of 2D films made from dodecylamine-coated CoPt nanoalloys deposited, as previously, either on amorphous carbon (Fig. 11.3A) or on HOPG (Fig. 11.3B). Here the nanoalloys were obtained by colloidal chemistry. They are 2 nm in size with a low size distribution (11%) [25]. The effects of the substrate on the organization was slightly different: the compactness of the monolayers increases as they are deposited on HOPG compared to the same NCs deposited on amorphous carbon. However in both cases the hexagonal organization is more local compared to larger (5 nm in diameter) silver NCs deposited on HOPG (Fig. 11.2A). This decrease in the ordering is due to a decrease in the interaction energy with the size of the NCs, as shown from Eq (1) and (2). The change in the compactness of the film is likely due to a change in the wettability of the substrate as the particle-substrate interaction does not change (carbon substrate in both cases). This is again due to the roughness of the substrates: the hydrophobicity of the substrate increases with its roughness [21]. Hence, with HOPG, the spreading of the droplet is lower than on amorphous carbon, yielding more compact structures after evaporation of the solvent.

Influence of the particle-substrate interaction

As seen previously, roughness and wettability of the substrates play important role on the self-organization process in the case of chemical syntheses because of the presence of the solvent. If we now consider different natures for the substrate, the wettability and the particle-substrate interaction have to be taken into account. Motte et al. notably reported dense and long-range organized monolayers made from dodecylthiols-capped Ag_2S (6 nm in diameter, 14% of size distribution) on HOPG substrate when smaller monolayer island with a lower particle density are obtained using MoS_2 as the substrate [13]. Moreover, 3D super-crystals made of Ag_2S NCs were observed in both cases. Nevertheless, they were isolated on the substrate in the case of HOPG, whereas they were on the NCs monolayers in the case of MoS_2 [13]. In both cases the roughness of the crystalline substrates was very low and similar. Therefore roughness cannot be held responsible for this difference. Wettability and particle-substrate interactions (which are not taken into account in

the Korgel model) have to be invoked instead. When the solvent containing capped NCs is deposited on the substrate, the whole surface is covered by the solution, evaporation occurs and the film gets thinner. At one point the behavior differs depending on the nature of the substrate: in the case of HOPG, the particle-substrate interaction strength, F, is repulsive (F= -0.4 x 10^{-5} dyn) while it is attractive with MoS_2 (F= 2.2 x 10^{-5} dyn). Thus, in case of HOPG, the substrate repels the nanocrystals even though the interparticle forces are attractive: this yields compact monolayers and, due to the capillarity effect during the evaporation process, isolated 3D super-crystals. Conversely, with MoS_2 as the substrate, and because the particles are subject to Brownian motion in the thin liquid film, they randomly collide with the substrate. Since the particle-substrate interaction is stronger than the interaction between nanoparticles (-25 kT compared to -1.25 kT), the NCs remain fixed on the surface. During evaporation of the solvent, surface diffusion could occur, and because the interparticle forces are attractive, this yields low-density interconnected monolayer domains separated by holes. Once MoS_2 is totally covered, the particle-substrate interactions do not play any more role and 3D aggregates can be formed by layer-by-layer growth.

Influence of the solvent on self-assembly processe.

One specificity of the chemical approach for self-assembly is the presence of a solvent. NCs are formed chemically, capped with ligand molecules and dispersed in solution [25]. Self-assemblies are then obtained by slow evaporation in presence of a substrate or by deposition of a drop of solution on a TEM grid. We have already seen that the wettability of the substrate plays an important role. However the solvent interacts also with the ligands surrounding the NCs and since the cohesion of the self-assembly results from the interaction between the organic chains surrounding the NCs, the way they are solvated (or not) by the solvent could also play an important role. Furthermore, the inter-particle interactions could be strongly dependent on the nature of the solvent. Figure 11-4 shows TEM patterns of the film obtained with 2 nm in size CoPt nanoparticles dispersed in different solvents and deposited on TEM grid coated by amorphous carbon.

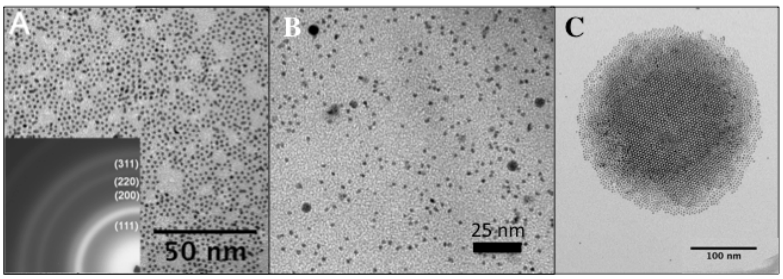

Fig. 11.4. TEM patterns of CoPt nanoalloys deposited on TEM grid coated by amorphous carbon. NCs are coated by dodecylamine and dispersed in (A) hexane; (B) 1-phenyl-octane; (C) toluene.

It is clear that the solvent can strongly disturb the self-organization process. If we compare hexane (Fig. 4A) and phenyl-octane (Fig. 4B), both are good solvents for the chains and the dispersion is highly stable, however their volatility markedly differs as hexane is highly volatil (boiling temperature, $T_{boiling}$, = 68°C; viscosity = 0.3 mPa.s) compared to 1-phenyl-octane ($T_{boiling}$ = 261°C; viscosity = 1.5 mPa.s). Furthermore, the high viscosity of phenyl-octane hinders the diffusion of the NCs at the surface in addition to the interdigitation between the ligands chains. As a result, no self-organized films can be observed using 1-phenyl octane as the solvent. In the case of toluene ($T_{boiling}$= 111°C, viscosity =0.6 mPa.s), 3D ordered self-assemblies can be observed (with a fcc structure) but not 2D monolayers. The viscosity is similar for toluene and hexane. Thus the diffusion is not responsible for this discrepancy. Indeed, this is due to a difference in the solvation of the capping chains [14,15]: Hexane is a very good solvent of the chains surrounding the nanoparticles conversely to toluene. As a consequence the inter-particle interactions are strongly modified (taking into account the vdW interactions between the ligands chains) [16]. Modeling of the inter-particles interaction in solution has been performed on similar systems including: (i) the van der Waals attraction between metallic cores; (ii) the free energy of mixing of the ligands with the solvent molecules; (iii) the elastic compression of these ligands [14]. It was shown that in toluene (a bad solvent of the capping chains) the inter-particles interactions are more attractive than in hexane (where in some cases, they can be repulsive) yielding some aggregation in solution, and thus the formation of 3D networks instead of the 2D monolayers obtained by using hexane as the solvent.

11.2.2- 3D self-organization of inorganic nanocrystals: Superlattices

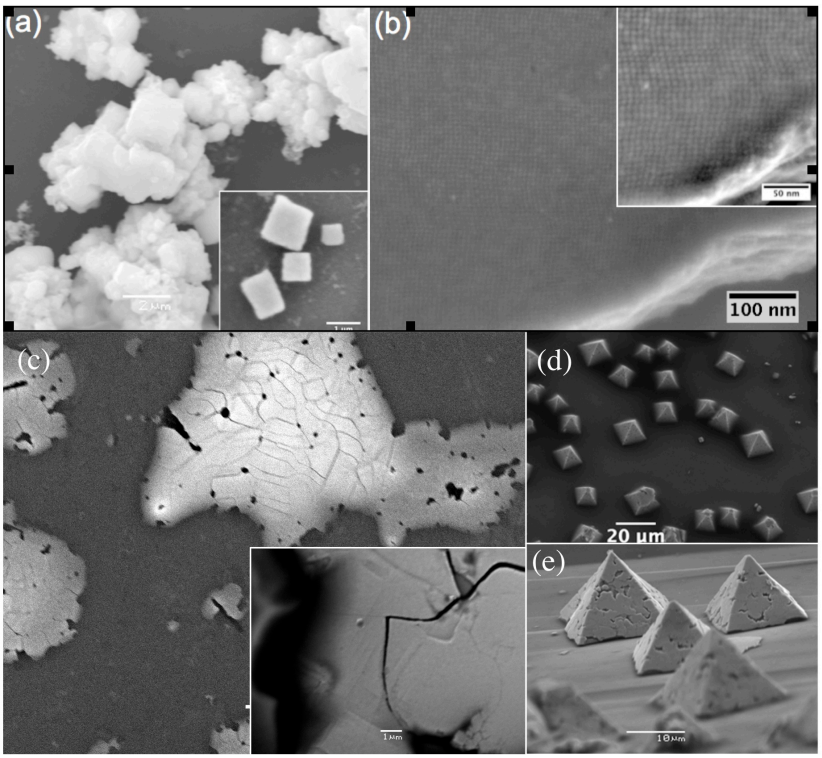

Fig. 11.5. SEM pattern of platinum NCs deposited on silicon substrates: (a) supperlatice of platinum nanocubes, which grew up in solution and deposited on the substrate during the evaporation; (b) HR-SEM image showing the self-organization of the nanocubes; (c) 3D superlattices made of truncated platinum nanocubes, which grew up on polished silicon; (d) 3D superlattices made of truncated platinum nanocubes, which grew up on rough silicon; (e) Magnification of (d); 3D film grown by immersion of a substrate and controlled evaporation of capped platinum NCs dispersed in toluene.

The assembly of NCs into extended 3D ordered superstructures has attracted much attention in the field of nanomaterials, both for fundamental studies and for potential devices. Chemical routes to self-assembly allows elaborating super-crystals with a 3D periodic organization of inorganic NCs. To our knowledge these is a specificity of the chemical approach since no 3D supperlattice has been obtained yet by the physical route. Since the NCs are dispersed in a solvent, it is easy to control the concentration of the NCs and thus the inter-particles interactions (see above). The crystallization of the 3D superlattice results from the arrangement of NCs in a periodic lattice during a slow evaporation process in presence of a substrate.
Crystal growth from solution is based on the existence of spontaneous formation of crystalline nuclei. The organization of nanostructures is based on the same general

growth rule in which the driving forces are different [27]. As with classical nucleation theory, in our case the super crystals can nucleate either heterogeneously onto the substrate or homogeneously into the colloidal solution itself [28]. In the nucleation stage, the formation of a "super seed" leads to the change of free energy ΔG defined by two contributions: (1) a bulk term, which expresses that the seed is more stable than the supersaturated solution of NCs; (2) a surface term, which takes into account the free-energy cost of creating a surface area of the new seed [29]. The condition of equilibrium between the super crystal and the NCs allow determining the nucleation energy barrier of the system, ΔG^{N}, which depends on $\Delta\mu$, the difference in chemical potentials between the super crystal and the NCs [30]. The crystal nucleation rate per unit volume, σ, is given by the following expression, where κ is the kinetic prefactor, T the temperature and k_b the Boltzmann constant:

$$\sigma = \kappa \exp\left(-\Delta G^{N} / k_b T\right)$$

For a growth from solution, the energy barrier for homogeneous nucleation, ΔG^{N}_{homo}, is higher than the corresponding value, ΔG^{N}_{hete}, for heterogeneous substrate-induced nucleation. Homogeneous nucleation occurs only when the solvent evaporation rate is sufficiently slow. However, the nucleation barrier ΔG^{N}_{homo} can also be overcome with some energetic input, for example through heating [31]. On the contrary, the nucleation barrier ΔG^{N}_{hete} is considered as being relatively low, therefore it is easy to overcome but at the same time also more dependent on interfacial properties. A significant competition between the two nucleation modes leads to aggregation of small superlattices in solution instead of the formation of supercrystals on the substrate. Furthermore, the interaction energies between nanoparticles, such as van der Waals and steric energies contribute to the free energy ΔG of the system [14,15]. As a result, a modification of interaction can induce a change of the growth process of super crystals. Thus, it is possible to tune the nucleation process of the superlattices in order to obtain either 3D film growing on the substrate (heterogeneous nucleation of the 3D superlattices, see for example Fig 11.4.C and Fig 11. 5. C and D) or 3D superlattices growing in solution and deposited on the substrate (homogeneous nucleation, see Figure 11. 5. A and B). Again there is no specificity of nanoalloys in comparison with homoatomic inorganic NCs. If we consider spherical NCs, the crystaline orientation are random and the whole pattern should be isotropic with a translational order, as a consequence their self-organization would probably result into compact packing structures such as face-centered cubic (fcc) or hexagonal close-packed (hcp). In order to obtain regular 3D superlattices, also called super-crystals, control of the deposition process is required. For this, the substrate (often silicon or HOPG) is directly immersed in the nanocrystal solution and the solvent (decane or toluene having a high boiling point, i.e. 174°C and 111°C, respectively) is allowed to evaporate. Solvent evaporation takes place under a slow flow of nitrogen. Because of its high boiling point, evaporation is slow and, depending on the substrate temperature (between 15°C and 50°C), this can take between two days and three weeks. After the solvent has evaporated and regardless

of the substrate temperature, scanning electron microscope imaging revealed a uniform film covering most of the substrate and with an average thickness of about 1 µm (see Fig.11. 5. C). It corresponds to a 3D film of several super-crystals composed of more than a hundred nanocrystal layers. The cracking behavior giving rise to sharp edges is the result of surface tension stresses arising during evaporation [32]. Control of the superlattice structure is not an easy task, and remains a work in progress. However, we can take advantage of the nature of the ligand or of the shape of the NCs to change the crystalline structure of the supperlattices. There is a clear analogy between the superlattices made of inorganic NCs as building blocks and the classical atomic crystals, even if the nature of the bond between the building blocks is drastically different. The structure and the interactions of the 3D superlattices can be characterized by associating different methods such as electronic microscopy, mainly electronic scanning microscopy at low (Fig 11. 5. a, c, d, e) or high resolution to reveal the organization (Fig. 11. 5. b) but also, more recently, electron tomography which can give a direct insight into the inner organization of the 3D superlattices [33, 34]. Grazing incidence small angle X-rays diffraction (SAXRD) can also be used to characterize the crystalline order of the 3D superlattices [35]

Crystalline structure of the 3D superlattices: influence of the capping agent

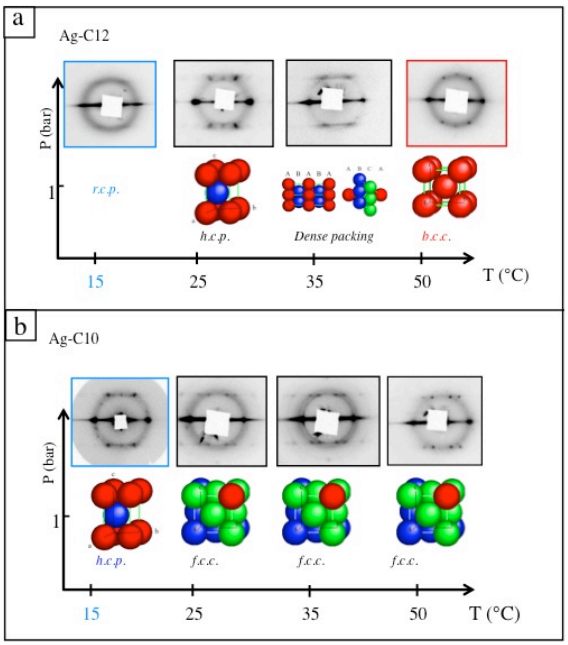

Fig. 11.6. Crystalline phase diagram of 3D self-assemblies made of silver NCs coated by a) dodecylthiol; and b) decylthiol. The crystalline order is characterized by SAXRD on a 3D film grown by immersion of a polished silicon substrate and after controlled evaporation of capped silver NCs dispersed in decane.

In the last decades, it has been shown that it is possible to control the type of super structures, either dense (hcp or fcc) or more open (body-centered cubic, bcc) by tuning the chain length of silver NCs capping agent [36]. This points towards the key role of the capping layer interactions in the stacking of spherical silver NCs. The relative ordering of the NCs in the 3D assemblies was investigated using SAXRD. Super-crystals made of silver nanoparticles coated by dodecylthiols with dense fcc or loose bcc structures as well as disordered arrangements depending on the deposition temperature (between 15 and 50°C) have all been identified (Fig. 11.6.a). These were attributed to equilibrium states, since they do not depend on the solvent evaporation rate and remain stable with the same large scale ordering over several months. When passivated by decylthiols (C10 chains) (with two fewer carbon atoms) the phase diagram is clearly different from that of Ag-C_{12} and only shows hcp and fcc structures (Fig. 11.5.b). This confirm the important role of the capping agent on the 3D super-lattices structure as it mediates the interactions between the NCs considered as the building blocks.

Crystalline structure of the 3D superlattices: Influence of the shape of the NC.

Another way to control the structure of the superlattices is to use non-spherical facetted NCs as building blocks. By experiencing anisotropic interactions, those NCs generate peculiar packings reflecting the particle's shape [37]. The development of synthetic methods allows us to control the shape, size and size distribution of the NCs [38] and thus to elaborate 2D or 3D superlattices with these anisotropic NCs. Let us discuss an example of this effect by considering the 3D supercrystals shown on Figure 11.5 [26]. Here supercrystals are made with either platinum nanocubes, 5 nm in size (Fig. 11.5 A and B) or with platinum cubo-octahedra (truncated nanocubes) also 5 nm in size (Fig. 11. 5 C, D and E). For nanocubes, SEM measurements showed cubic super-crystals that are mainly stacked in random positions (Fig. 11.5A) or more rarely isolated on the substrate (inset of Fig. 11.5A). Their typical lateral size is in the range of 0.5–2.0μm. Fig. 11.5 B shows the high-resolution SEM-FEG images of the nanocube organization in the simple cubic structure. It clearly exhibits a long-range order across almost 1 μm. In addition, in the HR-SEM image, the cubic arrangement reveals stacking faults, which are likely due either to local heterogeneities of the NC shapes or to a local perturbation of the growth process. It has been confirmed by SAXRD measurements that the crystalline structure is simple cubic with a lattice parameter around 8 nm [26]. If we now consider cuboctahedra, SEM images show the formation onto the substrate of domains of super-crystals having a pyramidal morphology with a square base (Fig. 11. 5 D and E). The normal to the substrate would be the (100) axis for pyramidal crystals. The size of the pyramids is of 12 μm with a size distribution of 20%. The angle between the normal to the substrate and the normal to the faces is around 45°.

SAXRD investigations have shown that conversely to the case of regular nanocubes, the diffraction spots correspond to specific orientations of pyramidal super-crystals on the substrate [26]. Furthermore the SAXRD patterns are perfectly accounted for with an fcc structure with a lattice parameter of a = 11.1 nm. Considering the shape of the NCs, we should expect a simple cubic structure for both the nanocubes and the cuboctaedra. The simple cubic structure is the most compact structure possible with cubic NCs (truncated or not) and the stacking should obey the rules of compactness already observed for spherical NCs. Actually, the fcc structure observed in case of cuboctaedra is surprising. Detailed analysis and modeling have shown recently that the fcc packing, which for cubes has a lower density than the simple cubic packing, is favored by the truncated nanocubes due to their Coulombic coupling by multipolar electrostatic fields, formed during a charge transfer between the ligands and the Pt cores [39]. Hence, we can see here both the effect of the shape on the structure of the 3D superlattices and the role of the ligand (i.e. the capping agent), which can change the structure of the superlattices.
The comparison between both cases shows also the difference in the nucleation processes depending on the NC shape, which comes from a difference in the metal core-core interaction. Those interactions are stronger for cubic NCs having only (100) facets than in the case of cuboctaedra, which have both (100) and (111) facets. As a consequence homogeneous nucleation is possible for nanocubes, whereas nuclei are not stable enough in the case of the cuboctaedra, giving rise to heterogenous nucleation and thus to the pyramidal structure if roughless silicon is used as the substrate.

3D superlattice: influence of the substrate

Figure 11.5. C shows a film of platinum cuboctahedra coated by dodecyl amine and deposited on polished silicon. Conversely to the case where rough silicon was used (Fig. 11.5. D and E), a large structureless film is obtained. As in case of 2D self-organization (see above), this probably results from a difference in wettability of the substrate in the case of heterogeneous nucleation. This favors the formation, on rough silicon, of small island of 2D superlattices where nucleation takes places on (100) facets yielding the pyramidal structure. Conversely, in the case of polished silicon the hydrophobicity decreases resulting into large and compact monolayers where the fcc superlattices can grow layer-by-layer without forming specific structures.
Another example of the effect of the substrate on the structure of 3D superlattices is shown in Figure 11.7: 3D superlattices were grown from suspensions of silver NCs. The process took place at the air-liquid interface, 5 mL of these nanoparticles dispersed in toluene ([Ag] = 2.10^{-3} M) being kept in a beaker under a saturated toluene atmosphere (see scheme in figure 11.7). After 7 days, flocculation of NCs occurred at the air saturated toluene interface, resulting in a thin interfacial film [40]. With increasing time, additional nanoparticles from the suspension were attracted by the first nanoparticles monolayer, thus inducing a progressive stacking of NCs layers to reach formation of well-defined fcc superlattices as characterized by SAXRD. The interfacial film, withdrawn using a tungsten ring, was deposited on HOPG (Figure 11 7. A and B) or gold (figure 11.7 C and D) substrates. Depending

on the wetting properties of the substrate, super-crystals of different morphologies could be obtained. On HOPG the solution was spread over the substrate. After evaporation of the solvent, the formation of a mixture of films and individual super-crystals with a well-defined triangular shape was observed. Gold presents a lower hydrophobicity than HOPG, which explains why a droplet was formed and, after evaporation of the solvent, individual super-crystals of well-defined triangular shape (triangular) were oberved.

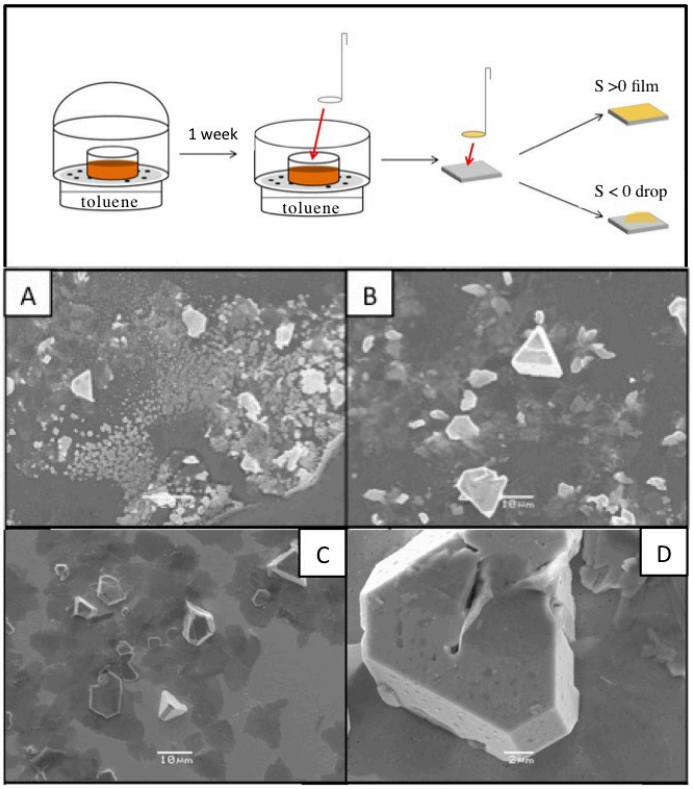

Fig. 11.7. SEM patterns of 3D superlattices made of dodecylthiol-capped silver nanocrystals obtained at the air-liquid interface and deposited (see scheme) on different substrate: (A) and (B) HOPG; (C) et (D) gold substrates.

3D superlattices: Influence of solvent

As seen above, the assembly of nanoparticles follows the same fundamental principle driving the crystallization of atomic or molecular crystals. The superlattices can thus grow either heterogeneously on a substrate or homogeneously in solution. The nature of the nucleation and growth process of superlattices depends not only on the

interparticle forces but also on the kinetics of the process. Homogeneous nucleation requires generally slow solvent evaporation that favors interparticle attraction. This can be promoted further by the addition of a poor solvent in the solution or by the presence of impurities [41,42]. Evidence has recently been provided about a change of the silver nanocrystal superlattice growth mode in hexane from heterogeneous to homogeneous character due to the presence of triphenylphosphine, coming from the decomposition of the silver precursor [43]. This observation is in agreement with simulations based on a Flory-type model, which shows that the interaction potential between the silver nanocrystals in the presence of triphenylphosphine changes from repulsive to attractive in hexane and more attractive in toluene (Figure 11.8).

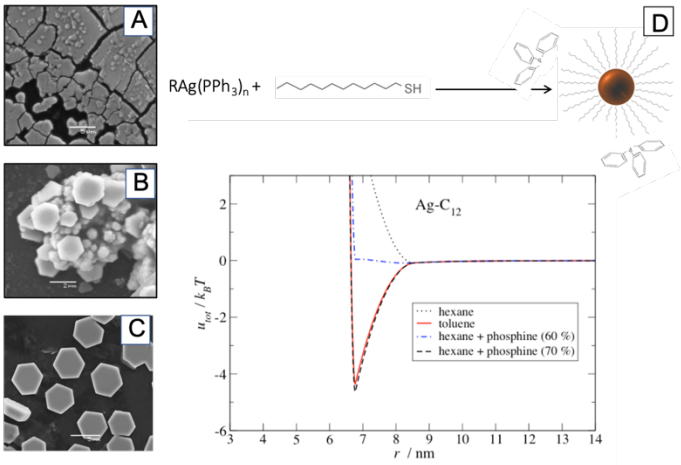

Fig. 11.8. SEM patterns of 3D superlattices made of silver nanocrystals coated by dodecanethiol: A) dispersed in pure hexane; B) in a mixture of hexane and phophine; and C) in pur toluene. D) Interaction potential between two silver nanocrystals (5 nmin diameter) coated by dodecanethiols in different solvents (toluene, hexane and mixtures of hexane and phosphine). All potentials were calculated at 25 °C.

11.2.3- 3D Binary superlattices

As shown before, there is no specificity of nanoalloys in the elaboration of the 2D or 3D superlattices, however there is the possibility to elaborate crystalline aggregates composed of one or more types of metallic or semiconductor or oxyde NCs [44]. This recent development of superlatices studies was encouraged by the investigation of the gem opals structure, which are made of bidisperse silica particles [45]. Nowadays, the self-assembly of nano-objects with various physical properties is an elegant and cheap bottom-up approach allowing to design multifunctional materials at the nanometric scale. This may open new routes to nanostructured materials with unique properties and these new nanostructured materials are of great interest for the development of potential applications in opto-electronics, high density data storage, catalysis, etc. We can consider this materials as a kind of super-alloy, which refers to situations where the alloying process involves entire monoatomic

NCs rather than atoms. Binary nanocrystal superlattices (BNSLs) can be described as materials made from the periodical arrangement of nanocrystals of different nature or size [46]. Moreover, the highly ordered structure and well-defined stoichiometry of the BNSLs permit a precise control of their properties. Hence, over the last decade, numerous BNSLs from metallic, metal-chalcogenide and metal-halogenide nanocrystals have been elaborated [47,48, 49] and a large number of binary materials with emergent properties in electronics [50], magnetism [51,52], optics [53] and catalysis[54] have been reported.

The mixture of binary nanoparticles is often presented as a mixture of hard particles yielding to a more densely packed that the pure 3D packing of nanoparticles: the second component often occupies an instersticial position in the compact structure (mainly fcc) of the first components. In entropy-driven crystallization and in the hard-sphere approximation, it is possible to predict the binary structures that are thermodynamically stable [55]. Thus there is two important parameters that can determine the possibility of formation of BNSLs with A and B components differing by their size: the radius ratio $\gamma = R_B/R_A$ with $R_A > R_B$ and the stoichiometry $x = n_B/(n_A+n_B)$. As a result the packing symmetry mainly depends on γ parameter. It should be noticed that in the case of capped nanoparticles the length L of the hydrocarboned chains surrounding the nanoparticles has to be taken into account as well, and the parameters γ becomes $\gamma_L = (R_B+L_B)/(R_A+L_A)$. The ratio γ allow to determine the domain of stability of the different structure. (Figure 11-9)

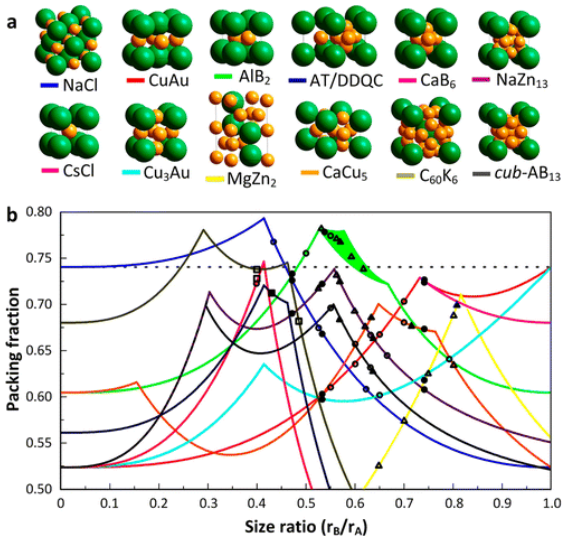

Fig. 11.-9 -Structural diversity of binary nanocrystal superlattices and low packing density predictions for most observed phases. (a) Models of 12 commonly observed binary arrangements showing larger A spheres in green and smaller B spheres in orange. Unit cells with AB, AB_2, AB_3, AB_5, AB_6, and AB_{13} stoichiometry as well as the structural motifs of Archimedean tiling (AT) and dodecagonal quasicrystal (DDQC) configurations are shown; (b) Plot of density vs size ratio for spheres packed in these arrangements. Overlay: data points showing phases observed in several BNSL studies using reported effective size ratios and densities predicted using sphere-packing

models. Most observed BNSLs appear to be open arrangements compared with close-packed monodisperse hard spheres (dotted line). [reproduced from ref 55 with permission].

However, even with this correction, the entropic model is not perfect and some experimental data do not agree with it. This could be due to a ligand effect depending of the molecular structure of the ligands. These thermodynamical effects are due to the short range soft repulsive interaction between the ligands [46]. It was notably reported that the crystalline structure of binary superlattices could depend also on the nature of the ligands [56].

Usually the methods to produce 2D or 3D binary superlattices are similar to those presented above. They have been successful to produce binary superlattices with different structures [57-59]. They are in general obtained in organic solvents and the attractive interactions between the nanocrystals (see above) limit the number of super-alloys and maintain their structure to compact lattices. Depending on their relative size, those can form binary 3D superlattices with precisely controlled stoichiometry and symmetry. As example Pileni et al. demonstrated that for binary superlattices made from colloidal cobalt and silver nanoparticles, the Ag/Co nanoparticle size ratio is the dominating factor in the formation of binary nanoparticle superlattices [60]. Figure 11.10 reported the different structures of binary superlattices obtained by self-assembly of silver and cobalt nanocrystals differing by their size. In agreement with the classical entropic model [55], the ratio γ governs the crystalline structure, even with these hydrocarbon-coated nanoparticles. However it was also shown that regardless of the relative ratio concentration of Co and Ag nanoparticles, the deposition temperature markedly changes the crystalline structure of binary superlattice.

Evidence has also been provided about the formation of binary 3D superlattices made of gold and silver NCs (5 nm in diameter) and having a diamond-like lattice [61]. The remarkable point is that these 3D binary superlattices have been obtained in polar solvent with NCs interacting via electrostatic forces (two types of NCs charged positively and negatively, respectively).

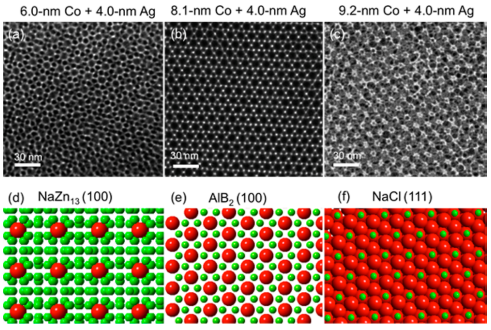

Figure 11.10: TEM images of binary nanoparticles superlattices formed under different values of the size ratio, keeping the other conditions constant (temperature, concentration ratio). [With permission of reference [60])

Besides metallic nanoparticles, different species of nanoparticles can be mixed, as thus obtained by mixing monodisperse colloidal semiconductor nanocrystals (PbS, CdSe, PbS/CdS; 4–11 nm) and giant polyoxometalate, POM. Again the crystalline structure are rationalized on the basis of dense packing principles of sterically stabilized particles with predominantly hard-sphere like interparticle interactions. By varying the size-ratios and relative concentrations of the constituents, the authors obtained known thermodynamically stable binary packings of hard-spheres such as NaCl, AlB_2, and $NaZn_{13}$ lattices and also $CaCu_5$-type lattice and aperiodic quasicrystals with 12-fold symmetry [62].

Recently Breitwieser et al. report modulation of the magnetic properties of superlattices by using giant polyoxometallate as a spacer in the superlattices of magnetic nanocrystals [63]. They formed BNSLs made of 2.9 nm $\{Mo_{132}\}$ POM mixed with maghemite (γ-Fe_2O_3) nanocrystals of 6.3 nm in size. In this case, conversely expected only AB structures were obtained. This confirms that the additional soft interaction between the ligands have to be taken into consideration. These experimental results obtained with similar systems illustrate the complexity of of modeling the structure of BNSLs.

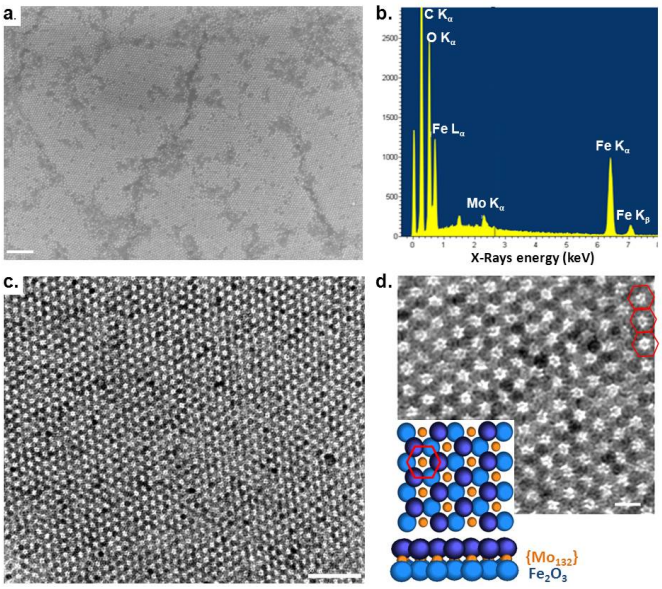

Figure 11.11. (a) FEG-SEM image of a DDA-{Mo132}/OA-g-Fe2O3 coassembly on HOPG (scale bar: 100 nm); (b) Energy dispersive X-ray spectroscopy from (a); (c) Typical TEM image of [111]-projected AB-type binary superlattice from a close-packed bi-layer of MNCs (scale bar: 50 nm); (d) Higher magnification TEM image of the AB-type binary superlattice (scale bar: 10 nm) together with the corresponding crystallographic models. [with permission

Despitesthe difficulties in their elaboration, these binary superlattices allow combining different NCs with different properties and may open new routes to nanostructured materials with unique properties.

11.3 Physical routes

As discussed in section 2, chemical routes have developed several tricks to narrow the natural size distribution and to obtain two-dimensional or three-dimensional arrays of mono or bimetallic nanoparticles. However, the presence of capping agents, mandatory for the self-organization process, can be a severe drawback for dedicated applications as catalysis. Moreover, the absence of epitaxial relationship with the substrate hinders the crystallographic orientation of the particles and does not allow using the epitaxial strain to tailor their properties. For example, it has been shown that the substrate induced strain could stabilize ordered alloys of immiscible elements [64], giving rise to completely new phase diagram at the nanoscale [65].
In this section, we show how a physical method, *i.e.* using physical vapor deposition on surfaces under vacuum, can also lead to self-organized nanoparticles, either mono or bimetallic. After a brief overview of the comparison between state-of-the-art top-down and bottom-up approaches for the specific case of bimetallic nanoparticles, we develop the concept of template surfaces and their use for the growth of ordered nanoparticles. While the most of the works in this field have focused on monometallic cases, we give few examples of bimetallic growth, either homogeneous alloy or core-shell nanoparticles. Finally, we give an overview of other physical techniques that can lead to original ordered arrays of bimetallic nanostructures.

11.3.1- Self-assembly versus top-down approaches: an overview

The top-down fabrication of nanostructures makes rapid progress and will soon meet length scales so far only accessible by bottom-up techniques. Advantages and disadvantages of the two approaches are evident. While the former enables arbitrary nanoparticle composition, shapes, and spacing, the latter is restricted to periodic particle patterns created by using template surfaces for the self-assembly. However, any lithographic techniques requires the use of masks, resists, or the transfer of patterns which might lead to chemical contamination that is absent in self-assembled particles.
Figure 11.12 shows nanostructure superlattices created by top-down approaches in the upper row compared with bottom-up approaches in the lower one. X-ray interference lithography (XIL) with extreme ultra violet (EUV) light was used to fabricate square lattices of Ni dots with 71 nm pitch, 55 nm diameter, and 40 nm height,

see Fig. 11.12a [66]. The technique used grating masks for the X-rays to create multiple beams generating an interference pattern on the polymer resist forming holes on the exposed areas that in the present case were filled by Ni using electrochemical deposition. Evidently, this filling can also be achieved with alloys or in sequences of several elements [67]. The technique is parallel, in the sense that the entire pattern is obtained on the resist with a single illumination. However, the grating mask has to be fabricated by e-beam lithography, therefore sequentially. Compared to e-beam lithography, the absence of proximity effect enables a very small spacing between the nanostructures. As an example of alloyed based nanoparticles, EUV-XIL could produce 50 nm CoPd multilayer capped SiO_x pillar arrays [68]. The ultimate resolution obtained is continuously improving, from 16 nm pitch [69] to 7 nm and below in the past years [70].

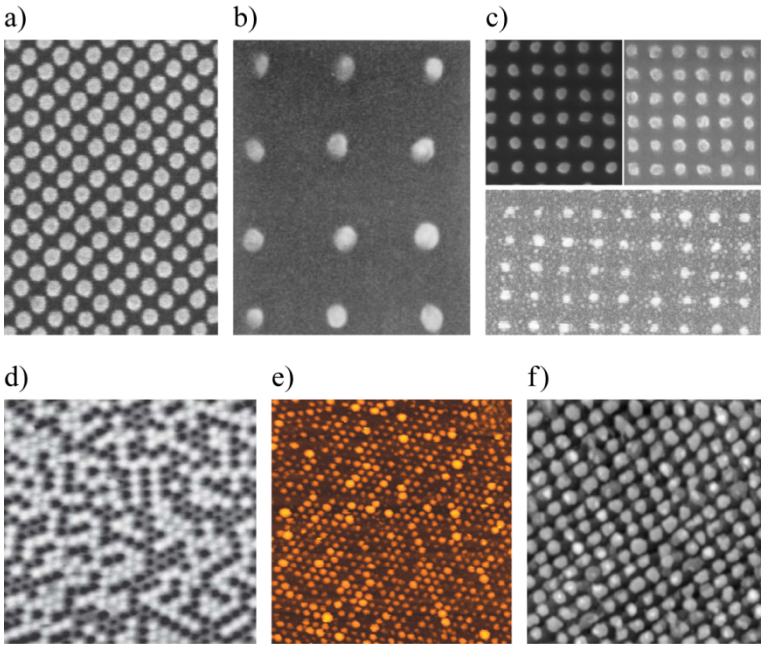

Fig. 11.12. a) XIL using 13 nm light to produce a superlattice of Ni dots with 55 nm diameter and 40 nm height, 1.0 μm scanning electron microscope (SEM) image [reproduced from ref 46 with permission]. b) 300 nm SEM image of square array of TiAu dots created by nanoimprint lithography [reproduced from ref 51 with permission]. c) 500 nm SEM images of Au (left) and Al (right) dots with 50 nm diameter and 100 nm pitch, as well as 25 diameter Au dots with 50 nm pitch (below) produced by nanostencil [reproduced from ref 52 with permission]. d) 10 μm magnetic force microscopy image of close packed monolayer of spherical polystyrene particles with 310 nm diameter covered by (0.3 nm Co 0.8 nm Pd)8 multilayer on 3 nm Pd seed layer [reproduced from ref 53 with permission]. e) 100 nm STM image of self-assembled Au/Pd particles obtained by deposition of 0.05 ML Pd seed followed by 0.40 ML Au at room temperature onto an $Al_2O_3/Ni_3Al(111)$-($\sqrt{67}$ x $\sqrt{67}$) surface [reproduced from ref 54 with permission]. f) 70 nm STM image of Co-core Fe-shell islands self-assembled on Au(11,12,12), pitch 7.2 nm along steps, 5.8 nm perpendicular.

Nanoimprint lithography molds into PMMA resist which is then developed by reactive ion etching taking away selectively the parts that have been compressed by the mold thus creating holes in the resist where the mold had protrusions. Subsequent metal deposition and lift-off leads to a pattern of metallic dots, such as the one shown in Fig. 11.12b. The dots consist of a 5 nm Ti layer recover by 15 nm Au, they have a diameter of 25 nm and the lattice has a pitch of 120 nm. This example is taken from the paper introducing this technique [71] in order to illustrate the resolution that could be already obtained at that time; more recent examples can be found in [76] and a review in [77]. Again, this technique is parallel and requires the fabrication of a mold in a serial process. A more direct technique is nanostencil, where a mask with the desired hole pattern is positioned in close proximity over a surface while exposed from the back to the atomic beam of the material to be deposited. Figure 11.12c shows 50 nm diameter Au and Al dots with 100 nm pitch, and, in the lower panel, 25 nm Au dots with 50 nm pitch [72]. In principle, the mask can also be scanned over the surface while depositing.

Colloid monolayer lithography [78] uses monodisperse colloid spheres that are assembled into a close packed monolayer that is either used as mask and then removed [79], or decorated from the top as shown on our example in Fig. 11.12d [73]. The fabrication of the colloidal particles is to a large extent top-down while the self-assembly of the monolayer is a bottom-up process. In our example the particles have been covered by a CoPd multilayer that is magnetically not connected between the individual particles, as demonstrated by the contrast in the magnetic force microscopy (MFM) image. Such a technique has been pushed far with FePt alloys to realize bit-patterned media for magnetic recording [80], but has not been transferred to a practical device level due to difficulties in the reliability and the scalability. The next example (Fig. 11.12e) shows a pure bottom-up approach for the fabrication of a hexagonal lattice of Pd-seeded Au particles with a pitch of only 4.2 nm using an Al_2O_3 film grown on a $Ni_3Al(111)$ surface as template [74]. The template function of this surface has been revealed in [81] and its structure has been identified as an oxide double layer with corner holes going all the way to the metal substrate [82]. These holes can be filled with Pd but due to the step edge barrier not with Fe, Co, or Au, thereby explaining why Pd seeding is needed to grow well-ordered superlattices of these elements. The final example (Fig. 11.12f) shows Co-core Fe-shell islands self-assembled on a Au(11,12,12) surface that provides a lattice of 7.2 nm x

5.8 nm nucleation sites created by the crossing of the partial surface disclocations of the Au(111) terraces with the steps [83]. Best order is achieved by depositing the Co core in 4 steps of 0.15 ML deposited at 150 K and annealed at 400 K. The 0.3 ML shell is deposited at 200 K with annealing to 300 K [75].

11.3.2- Self-organized nano-alloys on nanostructured crystalline substrates

11.3.2.1- Nanostructured crystalline surfaces as templates

In order to get a naturally ordered growth on surfaces, the basic idea is to start from a patterned surface that will serve as a template for a subsequent growth. Although this patterning can be obtained from lithographic techniques [84], the realization of nanometer size clusters on very dense arrays (typically below a periodicity of 10 nm) requires naturally patterned surfaces, also named self-organized crystalline surfaces. A broad range of materials and surface science phenomena can display mesoscopic periodic surface patterns and can therefore be suitable for subsequent ordered growth. Most of the early studies have focused on metallic surfaces [85] with the well-known Au(111) reconstructed surface [86]. More generally, the misfit parameter between a substrate and an ultrathin overlayer very often leads to a network of surface dislocations with patterns and periodicities depending on each system. The control of the period is rather delicate on these surfaces although it is clearly linked to the misfit parameter [87]. A clever way to vary continuously this period is to use a surface alloy with different concentrations to modify the misfit parameter following the Vegard law. Fig. 11.13a shows such an example of a dislocation network of a Au_xNi_{1-x} surface alloy on Ni(111). By changing the amount of Au on the surface and therefore the Au concentration of the surface alloy after annealing, it has been shown that the period can be varied continuously from 5 nm to 2.5 nm [88]. A drawback of these heteroepitaxial structures is that it is very difficult to obtain homogeneous patterns over a macroscopic surface, because of local fluctuations in coverage and defects like step edges. To circumvent this issue, it has been proposed to use vicinal surfaces, possibly together with dislocation networks, as Au(788) shown in Fig. 11.13b. This way, one can obtain nanometer scale patterned surfaces with coherency over a macroscopic scale, suitable for long-range ordered growth [89]. It is also worth noting that the periodicity perpendicular to the steps can be easily changed by choosing a different miscut angle. The principles and underlying physical processes of ordered growth on these two kinds of systems will be detailed in the next section.

Self-organized crystalline surfaces can also be made out of different materials like insulating layers, graphene sheets and molecular layers. Fig. 11.13c shows the submonolayer nitruration of a Cu(100) surface obtained by a controlled exposure to

atomic nitrogen. Due to strain relief in the surface layer, the c(2x2) copper nitride islands (appearing darker in the STM image) self-arrange in a square lattice with a 5 nm periodicity [90], which can be used for the subsequent growth of ordered metallic clusters at room temperature due to a very different sticking coefficient between nitride parts and bare copper parts [91]. In order to obtain a true electronic decoupling from the substrate, ultrathin insulating layers showing mesoscopic order can also be used, like in the case of Fig. 11.13d displaying the surface of a 2 ML alumina films on a $Ni_3Al(111)$ surface. This very regular pattern is due to the complex Al_20_3 atomic structure and its epitaxial relationship with the underlying substrate. It has been studied in details both by STM [82] and AFM [92]. It was shown that some adatoms like Pd or Pt can be trapped at room temperature on this regular lattice, giving rise to a nucleation seed for subsequent ordered growth, as shown in Fig. 11.8e where impressive arrays of monodisperse Au_xPd_{1-x} nanoparticles have been realized for future catalytic studies [74]. More recently, two-dimensional materials have also been proposed as templates for ordered growth. Firstly, epitaxial graphene on metals has been actively revisited for such a purpose [93,94]. On Ir(111), it was shown that a single domain moiré pattern can be obtained over at least several micrometres scale, irrespective of surface defects like step edges, as shown in Fig. 11. 9e [95]. More recently, ordered clusters of magnetic materials of interest like Ni [96] and Sm [97] have also been obtained with such moiré structures. Secondly, hegaxonal boron nitride on metals also shows moiré lattices of nanometer scale that can be used for ordered growth. At least Ir, C and Au depositions displays regular arrays of rather monodisperse clusters [98]. Another very active research area to achieve two-dimensional templates is the two-dimensional supramolecular chemistry with the goal to achieve fully controlled molecular networks adsorbed on a substrate. A nice organo-metallic example is shown in Fig. 11.13f, obtained by the deposition of NC-Ph3-CN linkers and the subsequent deposition of Co atoms on Ag(111) [99]. By adjusting accurately the amount of molecules and Co atoms on the surface, it is possible to form at least micrometer size domains of ordered molecular pores. A great advantage of these new self-organized surfaces is the possibility to change easily the lattice period with different linkers, typically in the range 3 to 7 nm pore diameter [100]. Depositing Co [101], Fe [102] or Bi [103] on such a template can indeed constrain the diffusion and therefore limit the nucleation and the size of the clusters. However, a drawback of such organo-metallic networks is that most of metals show a tendency to interact with the molecular moieties, what can affect the organization of the lattice. It is therefore more useful to organize or confine other molecules. It is worth noting that inorganic chemistry has also developed in the last decades numerous molecules with small clusters of metallic ions like Fe_4 or Mn_{12} that have interesting magnetic properties and can be also self-assembled on surfaces [104].

Although the physical mechanisms driving a mesoscopic ordering on surfaces are of high interest and still under investigation, our goal here is to show how to use such patterned surfaces for self-assembly of nano-alloys. In fact, as already shown

in Fig. 11.12, most of the surfaces of Fig. 11.13 have served for such a purpose with various simple materials. For example, the Au(788) surface has been used for the growth of two dimensional lattices of Co[88], C_{60} [106], Ag and Cu [107], Fe [108], etc. In very few model systems, the atomistic mechanisms responsible for ordered growth have been studied in detail [109,110], and the temperature dependence of the growth on patterned substrates has been analyzed [111]. In the following, we explain the basic concepts leading to ordered growth and our present understanding of such phenomena. We also discuss the specificity of making ordered bimetallic alloys, either in core-shell or mixed geometry, although experimental works are still scarce. It is worth noting that an important condition in order to obtain ordered growth is that the surface patterns should remain unaffected by the growth process. Considering the complexity of surface science phenomena, this issue point is not trivial and remains generally difficult to predict. This hypothesis will be assumed to be true in the following, although, few examples of self-organized surfaces modified during the growth of nanostructures have been reported [112,113].

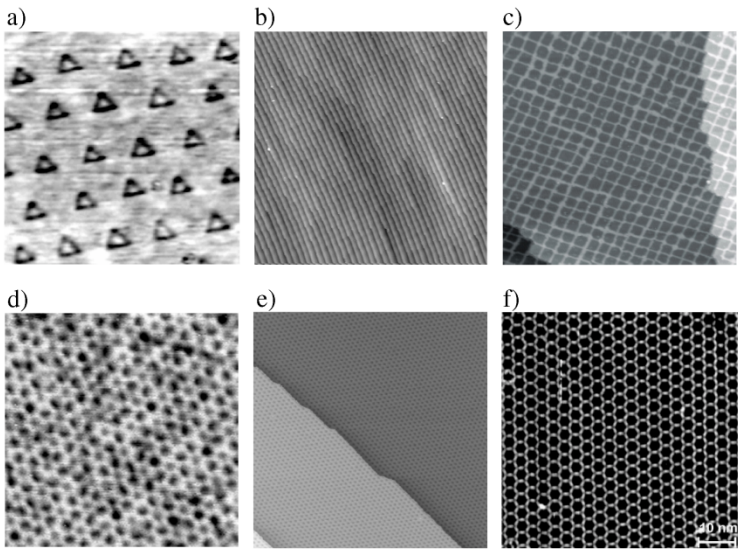

Fig. 11.13. a) 20 nm STM image of a network of misfit dislocations on a AuNi surface alloy created by the deposition of 0.35 ML of Au on Ni(111). Image taken from figure 11 of reference [reproduced from ref 67 with permission] b) 150 nm STM image of a Au(788) vicinal surface. The distance between step edges is 3.8 nm and can be controlled via the miscut angle. The period of the reconstruction perpendicular to the step edges is 7.2 nm. c) 100 nm STM image of a Cu(100) image covered by 0.45 ML of atomic nitrogen arranged in self-organized 5 nm squares of a c(2x2) structure. d) 36 nm STM image of a Al_2O_3 bilayer on $Ni_3Al(111)$. The period of the surstructure is 4.13 nm [105]. Courtesy of C. Henry, CiNaM, Marseille, France. e) 125 nm STM image of a graphene layer on Ir(111). The period of the hexagonal moiré pattern is 2.5 nm. Image taken from figure 3 of reference [reproduced from ref 74 with permission]. f) 65 nm STM image of a two-dimensional molecular network on Ag(111). The mean inner diameter of molecular pores is 3.4 nm. Image taken from figure 2 of reference [reproduced from ref 98 with permission].

1.3.2.2- The principles of ordered growth on nanostructured surfaces

Nucleation and growth of islands on surfaces has been extensively studied for many years and they are reviewed in articles or books [84,114]. Atoms are deposited from a vapor pressure onto a surface such as in the common case of solid on solid models. In case of adatoms moving on a homogeneous substrate (what we call homogeneous growth), the process is well described by a mean field theory and is essentially determined by atomistic parameters for surface diffusion and binding energies of adatoms to clusters. Values for these parameters may be determined by comparing scaling predictions with suitable experimental measurements [115]. A key experimental quantity for such a comparison is the cluster density versus the temperature that can be easily determined from variable temperature STM experiments. In the regime of complete condensation which is generally relevant for metal on metal growth at room temperature, re-evaporation of adatoms from the substrate onto the vapor is negligible. The logarithm of the cluster density as function of the inverse of temperature (Arrhenius plot) gives a straight line with a slope directly proportional to the diffusion energy E_d. This is valid in the case of stable dimers on the surface *i.e.* critical cluster size i=1 (i is defined as the atomic size of the biggest unstable cluster). At higher temperature, the critical nucleus size generally increases and this leads to a higher slope. Such behavior is also found in Kinetic Monte-Carlo (KMC) simulations. The advantage of a KMC simulation is that it goes beyond the mean field approximation which is known, for example, to overestimate the islands density. Another key quantity measurable experimentally and by KMC simulations is the size distribution which is found to be independent of temperature (cf. Fig. 11.14f) but narrows down when i>1 [116].

The nucleation and growth on heterogeneous surfaces such as the ones of Fig. 11.13 can also strongly narrow the size distribution. There are typically two kinds of mechanisms to get an ordered growth regime. The first one is that adatoms are repelled by an extended energy barrier that defines a unit cell. This is the case of most dislocation patterns (Fig. 11.13a), molecular networks (Fig. 11.13f) and certainly of moiré on graphene (Fig. 11.13e). The second mechanism is that some ordered atomic sites on the surface can be preferential for nucleation like on Au(788) (Fig. 11.13b) and Al_2O_3 films (Fig. 11.13d). Surprisingly, these two processes give rise

to the same results, as demonstrated in details for the case of Ag growth on 2 ML Ag/Pt(111) (Fig. 11.14a and b) and Co growth on Au(788) (Fig. 11.14c and d). Let us develop the second one, following a mean field point defect model [117,110]. Starting from rate equations for diffusion (E_d=0.12 eV) and nucleation of n-mers on a surface with a regular mesh of atomic traps (E_t=0.7 eV), the typical simulated curve of the logarithm of the critical cluster density versus inverse temperature is shown in Fig. 11.14d [111,114]. For the lowest temperature, no variation is found: the clusters density is constant with temperature. This corresponds to a low diffusion regime called "post-nucleation" [85] when adatoms hardly diffuse on the surface and are stable. Between 45 K and 80 K, a linear decrease of the cluster density with temperature in an Arrhenius plot is found. At such low temperatures, the adatoms mean free path on the surface is lower than the mean distance between traps. This regime is identical to the homogeneous growth and slope of the Arrhenius plot is E_d. Above the temperature threshold T_o, the system displays the ordered growth regime. The maximum cluster density is constant, equal to the density of traps. The value of T_o is therefore determined via E_d and the traps density n_t. The ordered growth occurs until T_e, as long as the typical energy E_t is sufficient to stabilize an adatom in a trap until a dimer nucleates. Above T_e, the critical island density decreases dramatically with temperature. The slope is higher than a simple homogeneous growth regime. Such a high value is mainly due to the long time spent by adatoms in traps. The effect of traps is then to reduce the effective diffusion length of adatoms [111]. Eventually, the mean field calculations including traps give a qualitative understanding of the ordered growth. Small diffusion energy and high trapping energy are the main ingredient to get an ordered growth over a large temperature range.

We now focus on the other key point of ordered growth, which is the achievement of narrow size distributions. Unfortunately, the mean field approach of the previous model cannot give any idea about the island size fluctuations during the nucleation and growth processes. Although Amar and Family [116] have proposed a phenomenological model for homogeneous growth, very little is known for the growth on heterogeneous substrates, especially for ordered growth. In order to obtain some information on these size distributions, KMC simulations can be performed [111]. Some results of these simulations are shown in Fig. 11.14e and f, which are for the case of a surface prestructured with a rectangular array of traps and a homogeneous surface. The homogeneous growth size distributions are perfectly reproduced by the Amar and Family model [116] for the case i=1 and show typical Full Widths at Half Maximum (FWHM) of 110%, whatever the temperature. In the case of ordered growth on a prestructured surface, the size distributions are narrower and are almost constant with temperature in this range. The FWHM for n_t=1/200 and a coverage of 0.1 ML is typically 50%. Interestingly, these size distributions are very well fitted by simple binomial distributions, as also shown for the case of growth on misfit dislocation patterns (see Fig. 11.14a) [109]. It is worth noting that simulations on randomly distributed atomic traps show a broadening of the island size distribution due to the distribution of traps Voronoi area. Consequently, the FWHM of the size distribution is generally limited to the perfectness of the traps array for a given coverage. In addition, for a perfect trap array, the intrinsic statistical limit to the size

distribution can only be reduced by increasing the coverage and/or using a surface with a lower trap density (larger Voronoi cells) [109].

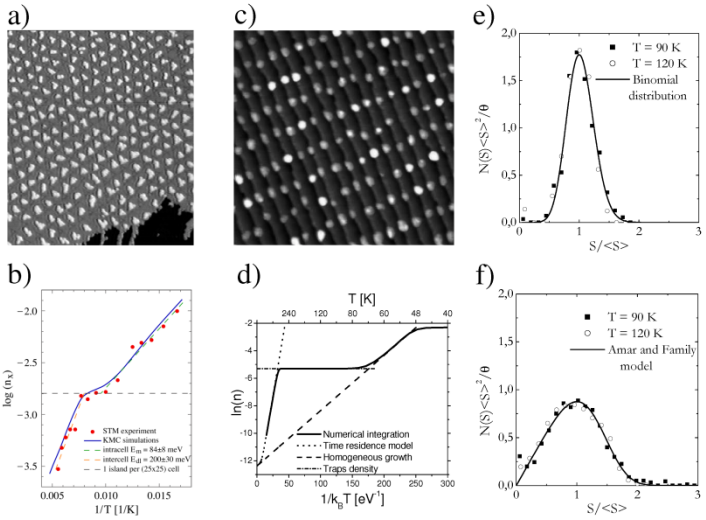

Fig. 11.14. a) 110 nm x 130 nm STM image of 0.1 ML of Ag deposited at 110 K on a misfit dislocation network, 2 ML Ag/Pt(111). b) Experimental Arrhenius plot (dots) with Kinetic Monte-Carlo simulation (full line) of the cluster density on the surface. c) 60 nm STM image of 0.2 ML of Co deposited at 130 K on the Au(788) surface. d) Arrhenius plot of the cluster density calculated by Kinetic Monte-Carlo simulations in the case of point defect nucleation with a trapping energy of 0.8 eV and a diffusion energy of 0.12 eV, corresponding to the experimental case of Co/Au(788). e) and f) Normalized size distributions at two deposition temperatures in the ordered growth regime (e) and the homogeneous growth regime (f), calculated by Kinetic Monte-Carlo simulations.

11.3.2.3- The specific case of bimetallic core-shell islands

For many elements the preparation of bi-metallic core-shell islands is non-trivial due to the tendency of insertion into the substrate or core, and the Ehrlich-Schwöbel barrier inhibiting descent of the shell element arriving on the core. Examples for islands with core-shell structures are illustrated in Fig. 11.15a-c.

The two first cases start from the ordered growth of Co on the herringbone reconstruction of the Au(111) surface. In Fig. 11.15a, Co dots (ordered white dots) of size 2-3 nm (0.35 ML) are surrounded by a Au capping (0.4 ML, light gray in the image). This case is rather favorable as Co and Au are immiscible elements and the Au surface energy is far lower than the Co one. Moreover, thermodynamics and kinetic

effects impose that the Co clusters are two layers high whereas the Au capping happens layer by layer [118]. It is therefore possible to control gradually the building of the complete Au shell and to link the structural and magnetic properties of such core-shell nanostructures [119]. It is also possible to circumvent thermodynamics by freezing the kinetic to obtain Co-Pt core-shell particle, like in Fig. 11.15b. The substrate is again Au(111) but the capping of the Co dots (0.5 ML) is now done with Pt. Whereas Co and Pt have a strong tendency to mix, it is possible, by deposition at room temperature to obtain a Pt annular structure around every Co nanostructure and compare, for example, their magnetic properties with the Co-Au case [120]. To demonstrate that playing with kinetic processes can lead to almost any desired structure, we show in Fig. 11.15c the reverse core-shell structure, i.e. Pt core with a Co rim. As Pt deposition on Au(111) does not lead to ordered growth [113], Pt is here deposited on Pt(111) and the nucleation is random. The desired density and size of the core are then defined by the Pt deposition temperature and coverage. At the experimental deposition flux of $F = 0.02$ ML/min Pt/Pt(111) the desired density of $n_x = 2.5 \times 10^{-4}$ islands/unit cell forms at a $T_{dep} = 200$ K, as inferred from inserting the diffusion barrier and pre-exponential factor of that system [121,122] into the scaling laws of nucleation [115]. However, limited mobility along steps gives rise to fractal island shapes for that system up to $T_{dep} = 400$ K [123]. In order to get a compact core the islands have to be annealed. This also leads to coarsening implying a slightly lower deposition temperature for the first step. The ideal parameters for Pt/Pt(111) are deposition at 170 K, followed by annealing at 770 K leading to compact monolayer Pt islands with a quasi-hexagonal thermodynamic equilibrium shape [123]. A two to three atoms wide rim is created around the Pt core by deposition of 0.15 ML Co at 220 K, (cf. Fig. 11.15c). In the STM images, Co and Pt can be discerned by their apparent height difference of about 30 pm. The Co deposition temperature has to be chosen high enough to inhibit nucleation of Co islands between and on-top of Pt islands. The first requirement is less stringent, one readily achieves $n_{x,Co} << n_{Pt\text{-}core}$, while the second requirement is in conflict with Co insertion into the Pt(111) surface starting at 180 K. The probability of second layer nucleation is essentially given by the Ehrlich-Schwöbel barrier [124-126] and has to be sufficiently low. Co insertion in the presence of Pt adatom islands takes place at slightly higher temperatures since the islands reduce the tensile stress of the Pt(111) surface. The temperature range constituting the best compromise between avoiding insertion and second layer nucleation is for the present system $200 \text{ K} \leq T_{dep,Co} \leq 260$ K [127]. Figure 11.15c shows that Co islands only occasionally grow on-top of the largest Pt islands.

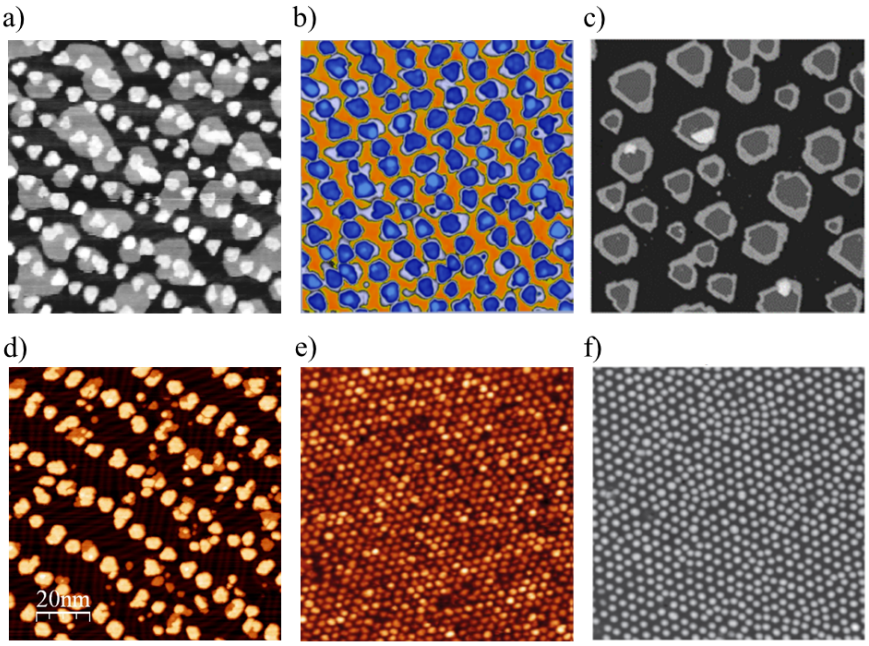

Fig. 11.15. STM images illustrating the realization of self-assembled core-shell, alloyed or pure nanoparticles a) Au(111) (50 nm, Θ_{Co} = 0.35 ML, Θ_{Au} = 0.4 ML). (b) Au(111) (100 nm, Θ_{Co} = 0.5 ML, Θ_{Pt} = 0.5 ML). (c) Pt(111) Co deposition at 220 K allows to decorate the Pt cores with thin Co rims (87 nm, $T_{dep,Pt}$ = 220 K, Θ_{Pt} = 0.25 ML, Θ_{Co} = 0.15 ML). (d) Alloy of 80% of Co and 20% of Pt (100 nm, Θ = 0.3 ML). (e) Sm nanoparticles on graphene on Ir(111) (75 nm, T_{dep} = 110 K, Θ = 0.08 ML). (f) Sm single adatoms on graphene on Ir(111) (65 nm, T_{dep} = 48 K, Θ = 0.01 ML).

Figure 11.16 illustrates the energy profile of a Co atom diffusing from the Pt core (left) over the Co rim down to the Pt terrace (right). The diffusion barriers on the Co(0001) and Pt(111) and faces differ slightly, however, the most important differences are the binding energies on both faces and the resulting barriers at the Co/Pt interline. Close inspection of Fig. 11.11d reveals that all the second layer nuclei are formed on the Pt side of the Pt/Co interline. This implies that the energy barrier of this line is higher for Co atoms coming from the Pt core than for the ones coming from the Co rim. This can only be achieved by a higher binding energy for single Co atoms on Pt than on 1 ML Co/Pt. Atoms landing on the Co rim can therefore reach the Pt core, or descend the Ehrlich-Schwöbel barrier to the Pt terrace below, while atoms arriving on the Pt core are confined there and back-reflected at the Co/Pt interline, where they have an increased density enhancing the likelihood of island formation at this location [128]. Co atoms coming from the Pt terrace attach to the rim and do not move up onto the Co monolayer rim. Note that at the beginning of the Co deposition, the Co atoms landing on the Pt core have to descend the Pt

edge towards the Pt terrace and overcome the respective Ehrlich-Schwöbel barrier not shown in Fig. 11.16.

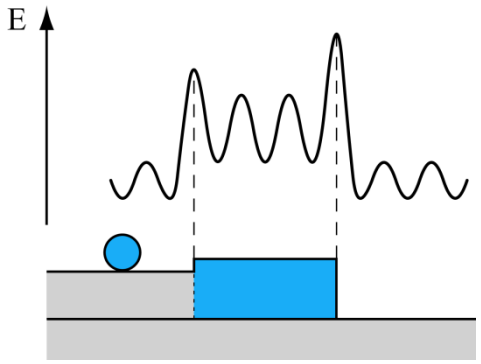

Fig. 11.16. Energy profile for a Co atom (blue) diffusing on a Pt core (gray) surrounded by a Co rim (blue) adsorbed onto a Pt(111) terrace (gray). Binding energy points down, the kinetic energy *E* to overcome the barriers points up. Right Ehrlich-Schwöbel barrier from Co ML down to Pt terrace; left: Pt/Co interline barrier.

The fact that the binding energy of Co on the Co rim is lower than on the Pt is only valid for single atoms, larger amounts of Co must be more stable on-top of Co since annealing of monolayer islands leads to the formation of double layer islands.
The principle outlined above for Pt-core Co-shell islands on Pt(111) has been used to evidence large magnetic anisotropies of step atoms [129], and has been transferred from Pt-core Co-shell islands to Co-core Au-shell islands on Au(111) [119] and Co-core Fe-shell islands on Au vicinal surfaces, see Fig. 11.12 above [75]. Recently, it has been used to reveal magnetic interline anisotropies for Fe/Co, Pd/Co and Pt/Co [130].
Bimetallic alloy islands with arbitrary composition can be created by co-depositing the two elements with the respective deposition fluxes. However, since each element has its own terrace diffusion barrier, varying the deposition fluxes also changes the particle density and therefore size. Using self-organized surfaces is a way to limit this density change as function of composition as the density of nucleation sites is predefined by the substrate. Fig. 11.15d shows a typical example of such a sample where Co and Pt have been codeposited on Au(111) [131]. The morphology is indeed very different from the sequential deposition (cf. Fig. 11.15b). Although the study of magnetic properties confirm that the nanostructures are mainly alloyed, we can still observe different morphologies, i.e. mono or bilayer islands (orange and yellow colors in Fig. 11.15d). Indeed, each element has its own barrier for diffusion along the atomic step of its own, the other element, or along a bi-metallic step, and therefore it can induce local variation of the concentration in a given element, giving rise to change in the morphology. Since low-coordinated step atoms often determine the magnetic and chemical properties, composition dependent studies require composition independent morphologies. This can be achieved by

using cores as nucleation sites for the creation of alloy rims [130]. This way, the rim morphology and evidently also the mean rim area remains constant and one can unequivocally trace the changes in the properties of interest back to composition and not to subtle morphology changes.

1.3.2.4- Towards few atoms clusters

It can be of interest to control the size of metallic clusters down to few atoms, both to study possible new quantum properties and for specific applications. For example, in magnetic recording, the $SmCo_5$ alloy is predicted to make stable nanomagnets at room temperature for grain size as low as 1.5 nm. The concept of ordered growth can be pushed down to low coverage to achieve very small clusters. Indeed, in the last years, nanodots of rare earth materials like Sm or Dy have been realized on the moiré patterns of graphene on Ir(111). Fig. 11.15e shows a typical image of ordered dots of Sm containing in average 9 atoms [97]. The same quality of order and size distribution can be retained until an average size of 50 atoms. An interesting question to address is how small can be the clusters with such an organization and a well-defined size. Due to the intrinsic statistical nature of nucleation and growth, even on self-organized surfaces, reaching the limit of single atoms with a good reproducibility from cell to cell is difficult. However, Fig. 11.15f shows an almost perfect lattice of Sm adatoms with a proportion of single atoms as high as 80% on a rather large temperature range of deposition. Such a result requires introducing a long-range repulsion between adatoms that is supposed to be electrostatic due to a charge transfer between Sm adatoms and the graphene [132]. Such samples are particularly suitable to explore the quantum reversal of magnetization in single atom magnetic bit [133].

11.3.3- Alternative approaches for the self-assembly of nano-alloys

11.3.3.1- Nanowires and sequential deposition

Up to now, we have only discussed the self-assembly of nanoparticles, with lateral dimensions in the range 1-5 nm and typically of atomic height. Another interesting class of nano-objects are nanowires, either for their electric, magnetic or optical properties. Several self-organized surfaces have a one-dimensional structure and can therefore lead to nanowires, down to a single atomic row. We can for example cite the case of CuO stripes on Cu(110) [134], of Si stripes on Ag(110) [135] and of numerous vicinal surfaces [136] where the distance between step edges is simply governed by the miscut angle with respect to a dense plane. Regarding alloys, such studies are more scarce excepting a pioneering work on Co-Ag alloy nanowires using Pt(111) stepped surfaces [137]. Another original way to obtain bimetallic nanowires on insulating substrates is through the substrate patterning by ion

sputtering at oblique angle. This leads to a rippled structure with a periodicity that can be tuned in a range typically between 10 and 100 nm by changing the substrate temperature and the incoming flux of sputtering ions. In the case of Fig. 11.17a, the substrate is an alumina film that has been sputtered by Xe ions at an angle of 55° with respect to the normal of the surface [138]. A codeposition of 1.4 nm of Fe and Pt is then performed at grazing angle, typically less than 5°, in order to take advantage of the shadowing effect of the ripples. After a post-annealing at 900 K, one obtains the nanowires on Fig.11.17a, where the contrast comes from the STEM-HAADF technique. Both high aspect ratio nanowires made of coalesced particles and isolated nanoparticles coexist on the surface. Such a sample allows studying the role of nanoscale confinement in the phase transition between the disordered and ordered FePt alloy with temperature and the magnetic properties of such objects by averaging techniques [138]. With the same spirit, the same group has made one-dimensional coupled Au_xAg_{1-x} nanoparticles to study their plasmonic properties, showing that the surface plamon resonance could be shifted with x [139] but that particles of pure metals exhibited a stronger field enhancement than the alloy [140].

All the nanostructures discussed so far have an aspect ratio that is flat, i.e. with lateral dimensions larger than their height, which is natural for physical vapour deposition techniques. Following some idea developed for the growth of self-assembled semiconductor quantum dots, it is however possible to grow nanostructures in the vertical dimension by a sequential deposition technique. A pioneering work was performed on the Co/Au(111) system where the alternate deposition of Co and Au at suitable temperature lead to Co nanopillars with an enhanced blocking temperature [141]. More recently, magnetic alloys nanowires embedded in an insulating matrix have been realized by pulse laser deposition and thoroughly analysed with different techniques. In this particular case (cf. Fig. 11.17b), the substrate ($SrTiO_3$) is not patterned and there is no lateral self-assembly. The ordered growth process with inhomogeneous nucleation has to be understood in the vertical direction where nanowires as long as 100 nm can be grown. Fig. 11.17b is a TEM top view image showing the density of $Co_{0.2}Ni_{0.8}$ nanowires and their diameter distribution, embedded in a matrix of $Sr_{0.5}Ba_{0.5}TiO_3$ [142]. The deposition process is sequential, as described in the following. Targets of CoO and NiO are sequentially shot by the pulsed laser, with a ratio of shots that fix the concentration of Co and Ni in the alloy. Snapshots of Kinetic Monte-Carlo simulations performed on a simpler system, i.e. Ni nanowires in a $SrTiO_3$ matrix (cf. Fig. 11.17c) help to understand better the growth mechanisms [143]. Once the homogeneous nucleation and growth of Ni on the substrate is done, a first step of Ostwald coarsening removes the smaller islands (in the present case, the substrate temperature is 870 K). The second step is to deposit the $SrTiO_3$ until the Ni islands are fully surrounded (cf. ii). Then, a new Ni deposition will mainly grow the Ni islands vertically and not nucleate new centres if the diffusion length is larger than the mean distance between islands, what can be adjusted with the substrate temperature and Ni flux. The layer-by-layer repetition of this process can lead in principle to nanowires as long as the deposited thickness. This technique is rather versatile and can in principle be applied to many different bimetallic

systems (see for example a recent study on CoAu nanowires [144]). Surprisingly, the quality of the epitaxy in such complex systems is very good, as checked by high resolution TEM image (cf. Fig. 11.17d) and by grazing incidence x-ray diffraction [145], allowing to tune the magneto-elastic anisotropy to control the magnetization direction within those wires. Based on the same idea, one can try to control the nucleation and growth and therefore the properties of functional materials like multiferroïc nanocomposites. In Fig. 11.17e for example, a growth of Cu nanopillars on $SrTiO_3$ was used to control the density and size of subsequent $CoFe_2O_4$ pillars in a $BiFeO_3$ matrix, modifying significantly their magnetic properties as compared to the homogeneous growth [146].

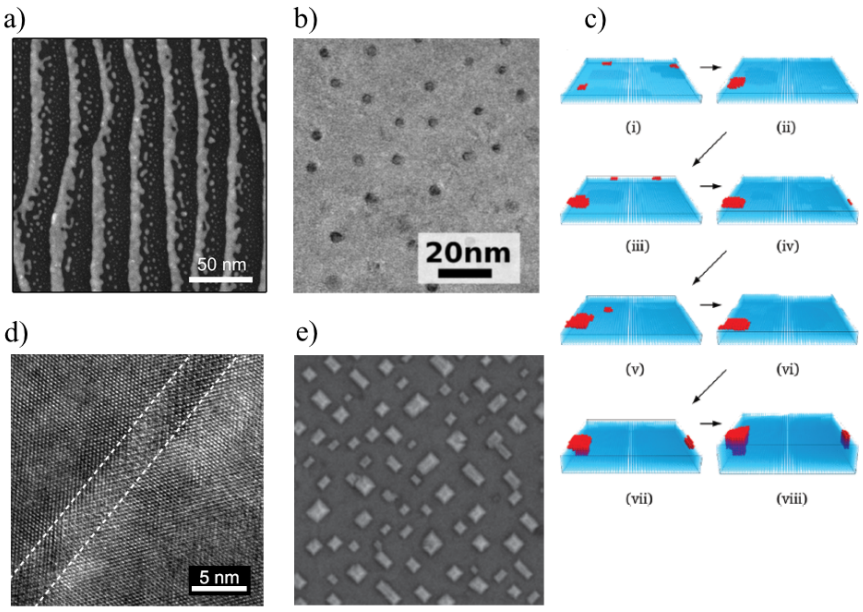

Fig. 11.17. a) STEM-HAADF image (200 nm) of 1.4 ML of FePt on a rippled alumina surface, after a post annealing at 870 K. b) Top view TEM image of $Co_{0.2}Ni_{0.8}$ self-assembled nanowires in a $Sr_{0.5}Ba_{0.5}TiO_3$ matrix. c) Schematic drawing of the sequential deposition technique leading to self-assembled buried nanowires. d) High resolution TEM image of a $Co_{0.32}Ni_{0.68}$ nanowire in a matrix of CeO_2. e) Top view SEM image (400 nm) of self-assembled $CoFe_2O_4$ pillars in a matrix of $BiFeO_3$.

11.3.3.2- Interactions in Low Energy Cluster Beam Depositions

Although most studies on the realization of ordered bimetallic nanostructures on a surface under vacuum are done using standard physical vapor deposition techniques as described above, a few others original ways have been developed. One of them

is the Low Energy Cluster Beam Deposition. In this technique, clusters are formed directly in the gas phase using for the condensation a supersonic expansion of an inert He gas [147]. Although this technique for production of nanoparticles is relatively heavy, it has several significant advantages. First, the highly out-of-equilibrium process of condensation allows achieving thermodynamically metastable alloys. Second, once ionized, these particles can be mass selected using a quadrupolar mass spectrometer, what can be used to select the size and possibly the exact composition of bimetallic clusters. Such nanoparticles of small kinetic energy (0.1 eV/atom) can be directly deposited on a surface, generally amorphous carbon or graphite, without fragmentation. Surprisingly, it was shown that nanometre size clusters show the same behavior of diffusion, nucleation and growth as single adatoms. Therefore, these objects could be spatially organized in principle using the patterned templates discussed in section 11.3.2.1, although it has not been tried yet to our knowledge. However, it has been discovered recently, that depending on the working pressure and the deposited material, clusters can be arranged at least locally in a dense array, as shown in Fig. 11.18a for 2 nm Pt particles [148]. Experiments with different materials (Pt or Au) and different base pressures [149] have shown that the local repulsion between neighboring clusters, at the origin of the organization, could be due to the adsorption of molecular species, possibly CO, at their surface. Since the surface reactivity depends drastically on the composition and size of bimetallic nano-alloys, the CO adsorption and the subsequent organization can change with the composition as shown for Pt_xAu_{1-x} nanoparticles (Fig. 11.18 a to d) [148], from nice arrays for pure Pt to coalesced ramified islands for pure Au. CoPt particles can also display a local assembly when small enough (Fig. 11.18e) while above 5 nm diameter the typical time of CO adsorption is smaller than the nucleation time and clusters coalesce (Fig. 11.18f), at least in ultra-high vacuum conditions [150]. In the future, by controlling the CO partial pressure during the deposition, it is highly possible that this technique can allow achieving dense arrays of highly monodisperse and controlled bimetallic nanoparticles. Finally, it is worth noting that this method of assembly, though in vacuum, is similar in principle to the chemical routes where the use of a chemical ligand around the particles hinders natural coalescence.

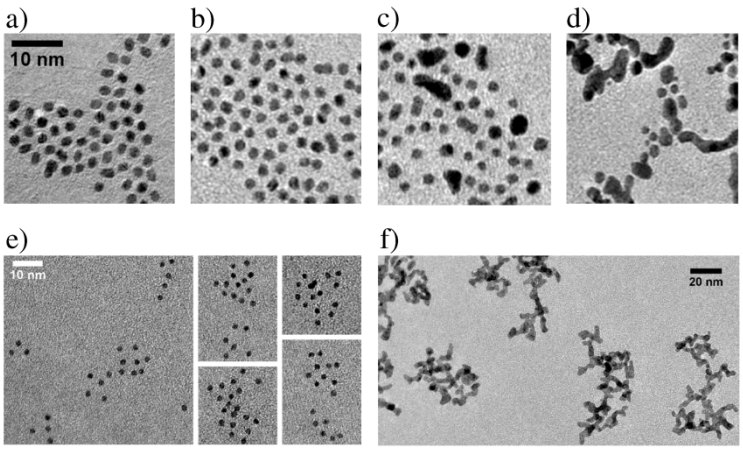

Fig. 11.18. Transmission Electron Microscope images. a) to d) Au_xPt_{1-x} 2.2 nm clusters deposited on amorphous carbon. a) x=0. b) x=0.2. c) x=0.5. d) x=1. Images taken from figure 1 of reference [103]. e) and f) CoPt clusters deposited on Highly Oriented Pyroelectric Graphite. e) 1.8 nm diameter. f) 5.8 nm diameter. Images taken from figures 3 and 4 of reference [reproduced from ref 150 with permission].

11.3.3.3- Buffer layer assisted growth and nanorings

Finally, we discuss growth methods where the nanostructures are created before they land on the surface. The first is buffer-layer assisted growth [151]. This technique condenses an inert gas buffer layer on the target substrate, then the constituent atoms of the nanoparticles are deposited onto this layer, subsequently this layer is evaporated and the deposited atoms diffuse towards each other and form clusters which then land softly on the surface after the last few monolayers of the inert gas have evaporated. This soft-landing method also works for pre-formed metal clusters [152]. An example of buffer-layer assisted growth of Co nanoparticles is illustrated in references [153,154]. The substrate is a hexagonal BN-monolayer on Rh(111) that forms a (12 *x* 12) moiré pattern acting as template for the clusters. Note that the direct deposition of transition metal atoms onto this surface does not lead to ordered growth [155]. For further examples of buffer layer assisted growth we refer to [156-160].

Well-ordered arrays of rings with nanometer diameter can be created by combining colloid monolayer layer lithography with evaporation under a certain angle. The ring diameter can be adjusted by the evaporation angle and the pitch by the diameter of the spheres forming the mask [161]. Alloy nanoparticles in solution have been arranged into rings with different diameter using polystyrene spheres with different size confining the solution by capillary forces to the interface between the spheres and the surface [162]. Ring diameters down to 85 nm can be achieved and the optical activity of the nanoparticles is preserved.

11.4-Conclusion and perspectives

In the bottom-up elaboration of new materials with specific properties, chemical and physical routes allow to fabricate nanostructured materials with a periodic organization. These 2D and 3D superlattices results from a controlled deposition or nucleation of NCs considered as building blocks on a substrates. We have reported here some overview on the elaboration of these superlattices and it should be noted besides the analogy in term of nucleation and growth of the superlattices, that the main difference between the chemical and the physical approach is the condition of elaboration of the superlattices. Nanocrystals are bare in the physical route, but coated by organic ligands in the chemical approach. This allows the elaboration of 3D structures which are not easy to fabricate by the physical route. However, these ligands could limit the integration of the superlattices in solid state devices as they can strongly modify the properties of the nanocrystals. This issue is more stringent the case in catalysis or electronic transport.
In both cases problems arise concerning the long term stability of the superlattices and the control of their structure. Future developments should be able to address these limitations especially in the case of superlattices of nanoalloys if we want to be able to control the NCs structure. At the moment the high temperature stability of the superlattices are low whatever is the mode of fabrication. We will have to control the stability at long times in order to develop new applications especially in the domains of data storage where superlattices made of nanoalloys could play an important role. Superlattices of nanoalloys have no real specificity compared to the monoatomic NCs. However, if we can control the organization of different NCs having different properties on the mesoscopic scale, either at 2D or 3D, a new kind of super-alloys could be elaborate with promising properties. It is one of the future direction for the self-assembly of inorganic NCs.

References :

[1] Pileni, M.P. (2001) Nanocrystals self assemblies: fabrication and collective properties, *J. Phys. Chem. B*, **105**, 3358-3372.
[2] Motte, L.; Courty, A.; Ngo, A-T.; Lisiecki, I. and Pileni, M.P., (2006) Self-Organization of Inorganic Nanocrystals*, in "Nanocrystals forming Mesoscopic Structures" M.P. Pileni Ed., Willey-VCH*, *Weinheim, Germany* pp. 1-47.
[3] Murray, C.B.; Kagan, C.R.; Bawendi, M.G. (2000) Synthesis and Characterization of Monodisperse Nanocrystals and Close-Packed Nanocrystal Assemblies, *Annu. Rev. Mater. Sci*. **30**, 545-610.
[4] Pileni, M.-P. (2007) Self-assembly of inorganic nanocrystals: Fabrication and collective intrinsic properties, *Acc. Chem. Res.,* **40**, 685-693
[5] Courty, A.; Mermet, A.; Albouy, P.A.; Duval, E.; Pileni, M.P. (2005) Vibrational coherence of self-organized silver nanocrystals in f.c.c. supra-crystals, *Nat. Mater*,**4** 395-398.
[6] Lisiecki, I.; Halte, V.;, Petit, C.; Pileni, M.-P.; Bigot J.-Y. (2008) Vibration dynamics of supra-crystals of cobalt nano-crystals studied with femtosecond laser pulses, *Adv. Mat*. 20, 1-4.
[7] Lisiecki, I. (2005) Size, Shape, and Structural Control of Metallic Nanocrystals, *J. Phys. Chem, B* **109**, 12231-12244.
[8] Podsiadlo, P.; Lee, B.; Prakapenka, V.B.; Krylova, G.V.; Schaller, R.D.; Demortière, A. and Shevchenko, E. (2011) High-Pressure Structural Stability and Elasticity of Supercrystals Self-Assembled from Nanocrystals, *Nano lett.,* **11**,579-588.
[9] Wang, Z.L. (1998) Structural Analysis of Self-Assembling Nanocrystal Superlattices, *Adv. Mater*. **10**, 13-30.
[10] Whetten, R.L.; Khoury, J.T.; Alvarez, M.; Murthy, S.; Vezma, I.; Wang, Z.L.; Stephens, P.W.; Cleveland, C.L.; Luetdtke, W.D. and Landman, U. (1996), Nanocrystal gold molecules, *Adv. Mater*. **8**, 428-433
[11] Prasad, B.L.V.; Sorensen, C.M.and Klabunde, K.J. (2008), Gold nanoparticles superlattices, *Chem. Soc. Rev*. **37**, 1871-1883
[12] Korgel, B.A.; Fullam, S.; Connolly, S.; and Fitzmaurice, D. (1998) Assembly and self-organization of silver nanocrystals superlattices: Ordered "soft spheres", *J. Phys. Chem. B* **102**, 8379-8388
[13] Motte, L.; Lacaze, E.; Maillard, M. and Pileni, M.P. (2000) Self-assemblies of silver sulfides nanocrystals on various substrates, *Langmuir* **16**, 3803-3812.
[14] Goubet, N.; Richardi, J. and Pileni, M.P. (2011) How to predict the Growth Mechanism of Supracrystals from Gold Nanocrystals, *J. Phys. Chem. Lett*. **2**, 417-422.
[15] Goubet N.; Richardi J. and Pileni, M.P. (2011) Which Forces Control Supracrystal Nucleation in Organic Media?", *Adv. Funct. Mater.,* **21**, 2693-2704.
[16] Luedtke, W.D. and Landman, U. (1996) Structure, Dynamics, and Thermodynamics of Passivated Gold Nanocrystallites and Their Assemblies, *J.Phys. Chem.* **100**, 13323-13329.
[17] Courty, A. (2010) Silver nanocrystals: self-organization and collective properties, *J.Phys.Chem.C,* **114,** 3719-3731.

[18] Goubet, N.; Portalès, H.; Yan, C.; Arfaoui, I.; Albouy, P.A.; Mermet, A. and Pileni, M.P. (2012) Simultaneous Growths of Gold Colloidal Crystals, *J.Am.Chem.Soc,* **134**, 3714-3719.
[19] Parker, D.; Lisiecki, I. and Pileni, M.P. (2010) Do 8 nm Co nanocrystals in long range ordered face-centered cubic supracrystals show superspin glass behavior?, *J. Phys. Chem. Lett.,* **1**, 1139-1142.
[20] Petrovski J.M.; Green, T.C. and El-Sayed, M.A. (2001) Self-Assembly of Platinum Nanoparticles of Various Size and Shape, *J. Phys. Chem A,* **105,** 5542-5553.
[21] Lu, M.H.; Song, T.; Zhou, T.J.; Wang, J.P.; Piramanayagam, S.N. Ma.; Gong, H. (2004) FePt and Fe nanocomposites by annealing self-assembled FePt Nanoparticles, *J Appl. Phys.* **95**, 6735-6737.
[22] Sun, S.H.; Murray, C.B.; Weller, D.; Folks, L. and Moser, A. (2000) Monodisperse FePt Nanoparticles and Ferromagnetic FePt Nanocrystal Superlattices, *Science,* **287**,1989-1992.
[23] Demortières, A. and Petit, C. (2007) First Synthesis by Liquid-Liquid Phase Transfer of Magnetic Co_xPt_{100-x} Nanoalloys, *Langmuir,* **23**, 8575-8584.
[24] Cai, Y.; Wolfkühler, D.; Myalitsin, A.; Perlich, J.; Meyer, A. and Klinke, C. (2011) Tunable electrical transport through annealed monolayers of monodisperse cobalt-platinum nanoparticles, *ACS Nano* **5**, 67-72.
[25] Petit, C. and Repain, V. (2012) Nucleation Growth of bimetallic nanoparticles in Nanoalloys : synthesis, structure and reactivity *Edited by Alloyeau D., Mottet C. and Ricolleau C.; (Springer London (2012)* pp.1-24.
[26] Demortière, A.; Launois, P.; Goubet, N.; Albouy, P.-A. and Petit, C. (2008) Shape-Controlled Platinum Nanocubes and Their Assembly into Two Dimensional and Three-Dimensional Superlattices, *J. Phys. Chem B*, **112**, 14583-14592.
[27] Lehn, J.-M. (2002) Toward complex matter: Supramolecular chemistry and self-organization, *Proc. Nat. Acad. Sci USA* **99**, 8, 4763-4768.
[28] Cölfen, H. and Mann, S. (2003) Higher-Order Organization by Mesoscale Self-Assembly and Transformation of Hybrid Nanostructures ,*Angew. Chem. Int. Ed.*, **42**, 2350-2365.
[29] Zaitseva, N.; Carman, L. (2001) Rapid growth of KDP-type crystals *Prog. Cryst. Growth Charact.* **43**, 1-118.
[30] Auer, S. and Frenkel, D. (2001) Suppression of crystal nucleation in polydisperse colloids due to increase of the surface free energy, *Nature,* **413**, 711-713.
[31] Sangwal, K. (1998) Growth kinetics and surface morphology of crystals grown from solutions: Recent observations and their interpretations, *Prog. Cryst. Growth Charact.* **36**, 163-248.
[32] Ngo, A. T.; Richardi, J . and Pileni, M. P. (2008) Do directional primary and secondary crack patterns in thin films of magnetic nanocrystals follow a universal scaling law?, *J. Phys. Chem. B* **112**, 14409-14414.
[33] Florea, I.; Demortière, A.; Petit, C.; Bulou, H.; Hirliman, C. and Ersen, O. (2012) 3D Quantitative Analysis of Platinum Nanocrystals Superlattices by Electron Tomography, *ACS Nano* **6**, 2574-2581.

[34] Friedrich, H.; de Jongh, P.E.; Verkleij, A.J.; de Jong, K.P. (2009) Electron Tomography for Heterogeneous Catalysts and Related Nanostructured Materials *Chem. Rev* **109**, 1613-1629.
[35] Lisiecki, I.; Albouy, P.-A. and Pileni, M.P. (2003) Face-Centered-Cubic "Supracrystals" of Cobalt Nanocrystals, *Adv. Mat.* **15**, 712-716.
[36] Henry, A.-I.; Courty, A.; Albouy, P-A.; Israelachvili, J. and Pileni M.P. (2008) Tunning of solid phase in silver supra-crystals made of silver nanocrystals, *Nano lett.* **8,** 2000-2005.
[37] Quan, A. and Fang, J. (2010) Superlattices with non-spherical building block, *Nano Today* **5**, 390-411.
[38] Complex-shaped metal nanoparticles: bottom-up synthesis and applications (2012) *edited by Sau T.K. and Rogach A.L. (Wiley-VCH, Weiheim, Germany 2012)*
[39] Chan, H.; Demortière, A.; Vukovic, L.; Kral, P. and Petit, C. (2012) Colloidal nanocube Supercrystals Stabilized by Multipolar Coulombic Coupling, *ACS Nano* **6,** 4203-4213.
[40] Andrieux-Ledier, A.; Albouy, P.-A. and Courty, A. (2013) Stability of Self-Ordered Thiol-Coated Silver Nanoparticles: Oxidative Environment Effects, *Langmuir* **29**, 13140-13145
[41] Ye, X.; Zhu, C.; Ercius, P.; Raja, S.N.; He, B.; Jones, M.R.; Hauwiller, M.R.; Liu, Y.; Xu, T. and Alivisatos A.P. (2015) Structural diversity in binary superlattices self-assembled from polymer-grafted nanocrystals, *Nature Comm*. **6**, 10052
[42] Si, K. J.; Chen, Y.; Shi, Q.; Cheng, W. (2018) Nanoparticle Superlattices: The Roles of Soft Ligands, *Advanced Science* **5**, 1700179.
[43] Ouhenia-Ouadahi, K.; Andrieux-Ledier, A.; Richardi, J.; Albouy, P.-A.; Beaunier, P.; Sutter, P.; Sutter, E.; Courty, A. (2016), Tuning the Growth Mode of 3D Silver Nanocrystal Superlattices by Triphenylphosphine, *Chemistry of Materials* **28**, 4380–4389.
[44] Redl, F.X.; Cho, K.S.; Murray, C.B. (2003) Three-dimensional binary superlattices of magnetic nanocrystals and semiconductor quantum dots, *Nature* **423**, 968-971.
[45] Murray, M. J.; Sanders, J. V. (1980) Close-Packed Structures of Spheres of Two Different Sizes II. The Packing Densities of Likely Arrangements, *Philos. Mag. A* **42**, 721–740.
[46] Boles, M.A.; Engel M. and Talapin D.T. (2016) Self-assembly of colloidal nanocrystals: from intricate structures to functional materials *Chem. Rev*. **116**, 11220-11289.
[47] Gaulding, E. A.; Diroll, B. T.; Goodwin, E. D.; Vrtis, Z. J.; Kagan, C. R.; Murray, C.B. (2015) Deposition of wafer-scale single-component and binary nanocrystal superlattice thin films via dip-coating, *Adv. Mat*., **27,** 2846-2851.
[48] Paik, T.; Murray, C. B. (2013) Shape-Directed Binary Assembly of Anisotropic Nanoplates: A Nanocrystal Puzzle with Shape-Complementary Building Blocks, *Nano Lett*. **13**, 2952-2956.
[49] Zheng, T.; Sun, L. D.; Zhou, J. C.; Feng, W.; Zhang, C.; Yan, C. H. (2013) Construction of $NaREF_4$-based binary and bilayer nanocrystal assemblies, *Chem. Commun*. **49**, 5799-5801.

[50] Urban, J. J.; Talapin, D. V.; Shevchenko, E. V.; Kagan, C. R.; Murray, C. B. (2007) Synergism in binary nanocrystal superlattices leads to enhanced p-type conductivity in self-assembled PbTe/Ag_2Te thin films, *Nat. Mater.* **6**, 115-121.
[51] Zeng, H.; Li, J.; Liu, J. P.; Wang, Z. L.; Sun, S. H. (2002) Exchange-coupled nanocomposite magnets by nanoparticle self-assembly, *Nature* **420**, 395-398.
[52] Chen, J.; Ye, X. C.; Oh, S. J.; Kikkawa, J. M.; Kagan, C. R.; Murray, C. B. (2013) Bistable Magnetoresistance Switching in Exchange-Coupled $CoFe_2O_4$–Fe_3O_4 Binary Nanocrystal Superlattices by Self-Assembly and Thermal Annealing, *ACS Nano* **7**, 1478-1486.
[53] Ye, X. C.; Chen, J.; Diroll, B. T.; Murray, C. B.; (2013) Tunable Plasmonic Coupling in Self-Assembled Binary Nanocrystal Superlattices Studied by Correlated Optical Microspectrophotometry and Electron Microscopy, *Nano Lett.* **13**, 1291-1297.
[54] Kang, Y. J.;. Ye, X. C.; Chen, J.; Cai, Y.; Diaz, R. E.; Adzic, R. R.; Stach, E. A.; Murray, C. B. (2013) Engineering Catalytic Contacts and Thermal Stability: Gold/Iron Oxide Binary Nanocrystal Superlattices for CO Oxidation, *J. Am. Chem. Soc.* **135**, 1499-1505.
[55] Boles, M.A. and Talapin, D.V. (2015) Many-Body Effects in Nanocrystal Superlattices: Departure from Sphere Packing Explains Stability of Binary Phases, *J. Am. Chem. Soc.* **137**, 4494–4502.
[56] Wei, J.; Schaeffer, N.; Pileni, M.-P. (2015) Ligand Exchange Governs the Crystal Structures in Binary Nanocrystal Superlattices, *J. Am. Chem. Soc.* **137**, 14773-14784.
[57] Saunders A.E.; Korgel, B.A. (2005) Observation of an AB Phase in Bidisperse Nanocrystal Superlattices *ChemPhysChem* **6**, 61-65.
[58] Shevchenko, E.V.; Talapin, D.V. Kotov, N.A. O'Brien S.; Murray, C.B. (2006) Structural diversity in binary nanoparticles superlattices, *Nature*, **439**, 55-59.
[59] Rogach, A.L. (2004) Binary Superlattices of Nanoparticles: Self-Assembly Leads to "Metamaterials", *Angew. Chem. Int. Ed.* **43**, 148-149.
[60] Yang, Z.; Wei, J.; Pileni, M.-P. (2015) Metal-Metal Binary Nanoparticle Superlattices: A Case Study of Mixing Co and Ag Nanoparticles, *Chemistry of Materials*, 27, 2152–2157.
[61] Bodnarchuk, M. I.; Krumeich, R. E.F.; Kovalenko, M.V.; (2013) Binary Superlattices from Colloidal Nanocrystals and Giant Polyoxometalate Clusters *Nano Lett.* **13**,1699-1705.
[62] Breitwieser, R.; Auvray, T.; Volatron, F.; Salzemann, C.; Ngo, A.-T.; Albouy, P.-A.; Proust, A. and Petit, C. (2015) Binary Superlattices from $\{Mo_{132}\}$ Polyoxometalates and Maghemite Nanocrystals: Long-Range Ordering and Fine-Tuning of Dipole Interactions, *Small* **12,** 220-228.
[63] Kalsin, A.M.; Fiallkowski, M.; Paszewski, M.; Smoukov, S.K.; Bishop, K.J.M.; Grzybowski, B.A. (2006) Electrostatic self-assembly of binary nanoparticle crystals with a diamond-like lattice, *Science* **312,** 420-424.
[64] Mehendale, S., Girard, Y., Repain, V., Chacon, C., Lagoute, J., Rousset, S., Marathe, M., Narasimhan, S. (2010). Ordered Surface Alloy of Bulk-Immiscible Components Stabilized by Magnetism. *Phys. Rev. Lett.* **105**, 056101.

[65] Marie, J.-B., Bellec, A., Chacon, C., Girard, Y., Lagoute, J., Repain, V., Rousset, S., Garreau, Y., Coati, A. (2016). Order-disorder phase transition in Au_2Fe on Ru(0001). *Phys. Rev. B* **94**, 235440.
[66] Heyderman, L. J.; Solak, H. H; David, C.; Atkinson, D.; Cowburn, R. P. and Nolting, F. (2004) Arrays of nanoscale magnetic dots: Fabrication by x-ray interference lithography and characterization. *Appl. Phys. Lett.,* **85**, 4989-4991.
[67] Blondel, A.; Meier, J. P.; Doudin, B. and Ansermet, J. P. (1994) Giant magnetoresistance of nanowires of multilayers. *Appl. Phys. Lett.,* **65**, 3019-3021.
[68] Auzelyte, V.; Dais, C.; Farquet, P.; Grützmacher, D.; Heyderman, L. J.; Luo, F.; Olliges, S.; Padeste, C.; Sahoo, P. K.; Thomson, T.; Turchanin, A.; David, C. and Solak, H. H. (2009) Extreme ultraviolet interference lithography at the Paul Scherrer Institut. *J. Micro/Nanolith. MEMS MOEMS*, **82**, 021204.
[69] Päivänranta, B.; Langner, A.; Kirk, E.; David, C. and Ekinci, Y. (2011) Sub-10 nm patterning using EUV interference lithography, *Nanotechnol.*, **22**, 375302.
[70] Mojarad, N.; Hojeij, M.; Wang, L.; Gobrecht, J. and Ekinci Y. (2015) Single-digit-resolution nanopatterning with extreme ultraviolet light for the 2.5 nm technology node and beyond, *Nanoscale*, **7**, 4031.
[71] Chou, S. Y; Krauss, P. R. and Renstrom, P. J. (1996) Imprint Lithography with 25-Nanometer Resolution, *Science*, **272**, 85-87.
[72] Vazquez-Mena, O.; Sannomiya, T.; Tosun, M.; Villanueva, L. G.; Savu, V.; Voros, J. and Brugger, J. (2012) High-Resolution Resistless Nanopatterning on Polymer and Flexible Substrates for Plasmonic Biosensing Using Stencil Masks, *ACS Nano*, **6**, 5474-5481.
[73] Albrecht, M.; Hu, G.; Guhr, I. L.; Ulbrich, T. C.; Boneberg, J.; Leiderer, P. and Schatz, G. (2005) Magnetic multilayers on nanospheres, *Nat. Mater.*, **4**, 203-283.
[74] Hamm, G.; Becker, C.; and Henry, C.R. (2006) Bimetallic Pd–Au nanocluster arrays grown on nanostructured alumina templates. *Nanotechnology*, **17**, 1943-1947.
[75] Brune, H. Private communication.
[76] Yang, J. J.; Pickett, M. D.; Li, X. M.; Ohlberg, D. A. A.; Stewart, D. R. and Williams, R. S. (2008) Memristive switching mechanism for metal/oxide/metal nanodevices, *Nat. Nanotechnol.*, **3**, 429-433.
[77] Nie, Z. H. and Kumacheva, E. (2008) Patterning surfaces with functional polymers, *Nat. Mater.*, **7**, 277-290.
[78] Deckman, H. W. and Dunsmuir, J. H. (1982) Natural Lithography, *Appl. Phys. Lett.*, **41**, 377-379.
[79] Burmeister, F.; Badowsky, W.; Braun, T.; Wierprich, S.; Boneberg, J. and Leiderer, P. (1999) Colloid monolayer lithography - A flexible approach for nanostructuring of surfaces, *Appl. Surf. Sci.*, **144-145**, 461-466.
[80] Albrecht, M., Makarov, D. (2012). Magnetic Films on Nanoparticle Arrays. *The Open Surf. Sci. Journal* **4**, 42-54.
[81] Degen, S.; Becker, C. and Wandelt, K. (2004) Thin alumina films on Ni3Al(111): A template for nanostructured Pd cluster growth, *Faraday Discuss.*, **125**, 343-356.

[82] Schmid, M.; Kresse, G.; Buchsbaum, A.; Napetschnig, E.; Gritschneder, S.; Reichling, M. and Varga, P. (2007) Nanotemplate with Holes: Ultrathin Alumina on $Ni_3Al(111)$. *Phys. Rev. Lett.*, **99**, 196104.
[83] Carbone, C.; Gardonio, S.; Moras, P.; Lounis, S.; Heide, M.; Bihlmayer, G.; Atodiresei, N.; Dederichs, P. H.; Blügel, S.; Vlaic, S.; Lehnert, A.; Ouazi, S.; Rusponi, S.; Brune, H.; Honolka, J.; Enders, A.; Kern, K.; Stepanow, S.; Krull, C.; Balashov, T.; Mugarza, A. and Gambardella, P. (2011) Self-Assembled Nanometer-Scale Magnetic Networks on Surfaces: Fundamental Interactions and Functional Properties, *Adv. Funct. Mater.*, **21**, 1212-1228.
[84] Eymery, J.; Biasiol, G.; Kapon, E.; and Ogino, T. (2005) Nanometric artificial structuring of semiconductor surfaces for crystalline growth, *C. R. Physique*, **6**, 105-116.
[85] Brune, H. (1998) Microscopic view of epitaxial metal growth: nucleation and aggregation. *Surf. Sci. Rep.*, **31**, 121-229.
[86] Chambliss, D.D.; Wilson, R.J.; and Chiang, S. (1991) Nucleation of ordered Ni island arrays on Au(111) by surface-lattice dislocations. *Phys. Rev. Lett.*, **66**, 1721-1724.
[87] Frank, F.C. and van der Merwe, J.H. (1949) One-Dimensional Dislocations. I. Static Theory. *Proc. R. Soc. Lond. A*, **198**, 205-216.
[88] Besenbacher, F.; Nielsen, L.P.,;and Sprunger, P.T. (1997) Surface Alloying in Heteroepitaxial Metal-on-Metal Growth in Growth and Properties of Ultrathin Epitaxial Layers. *Edited by D. A. King and D. P. Woodruff (Elsevier Science, Amsterdam, 1997)*, **8**, 207-257.
[89] Repain, V.; Baudot, G.; Ellmer, H. and Rousset, S. (2002) Two-dimensional long-range–ordered growth of uniform cobalt nanostructures on a Au(111) vicinal template, *Europhys. Lett.*, **58**, 730-736.
[90] Rousset, S.; Croset, B.; Girard, Y.; Prévot, G.; Repain, V. and Rohart, S. (2005) Self-organized epitaxial growth on spontaneously nano-patterned templates. *C. R. Physique*, **6**, 33-46.
[91] Ellmer, H.; Repain, V.; Sotto, M. and Rousset, S. (2002) Pre-structured metallic template for the growth of ordered, square-based nanodots, *Surf. Sci.*, **511**, 183-189.
[92] Hamm, G.; Barth, C.; Becker, C.; Wandelt, K. and Henry, C.R. (2006) Surface Structure of an Ultrathin Alumina Film on $Ni_3Al(111)$: A Dynamic Scanning Force Microscopy Study. *Phys. Rev. Lett.*, **97**, 126106.
[93] N'Diaye, A.T.; Bleikamp, S.; Feibelman, P.J.; and Michely, T. (2006) Two-Dimensional Ir Cluster Lattice on a Graphene Moiré on Ir(111). *Phys. Rev. Lett.*, **97**, 215501.
[94] N'Diaye, A.T.; Gerber, T.; Busse, C.; Mysliveček, J.; Coraux, J. and Michely, T. (2009) A versatile fabrication method for cluster superlattices, *New J. Phys.*, **11**, 103045.
[95] Coraux, J.; N'Diaye, A.T.; Busse, C. and Michely, T. (2008) Structural Coherency of Graphene on Ir(111). *Nanoletters*, **8**, 565-570.
[96] Sicot, M., Bouvron, S., Zander, O., Rüdiger, U., Dedkov, Y.S., Fonin, M. (2010). Nucleation and growth of nickel nanoclusters on graphene Moiré on Rh(111). *Appl. Phys. Lett.* **96**, 093115.

[97] Mousadakos, D., Pivetta, M., Brune, H., Rusponi, S. (2017). Sm cluster superlattice on graphene/Ir(111). *New J. Phys.* **19**, 123021.
[98] Will, M., Atodiresei, N., Caciuc, V., Valerius, P., Herbig, C., Michely, T. (2018). A Monolayer of Hexagonal Boron Nitride on Ir(111) as a Template for Cluster Superlattices. *ACS Nano* **12**, 6871–6880.
[99] Schlickum, U.; Decker, R.; Klappenberger, F.; Zoppellaro, G.; Klyatskaya, S.; Ruben, M.; Silanes, I.; Arnau, A.; Kern, K.; Brune, H. and Barth, J.V. (2007) Metal-Organic Honeycomb Nanomeshes with Tunable Cavity Size. *Nanoletters*, **7**, 3813-3817.
[100] Kühne, D.; Klappenberger, F.; Decker, R.; Schlickum, U.; Brune, H.; Klyatskaya, S.; Ruben, M. and Barth, J.V. (2009) High-Quality 2D Metal-Organic Coordination Network Providing Giant Cavities within Mesoscale Domains. *J. Am. Chem. Soc.*, **131**, 3881-3883.
[101] Krenner, W., Klappenberger, F., Kühne, D., Diller, K., Qu, Z.-R., Ruben, M., Barth, J.V. (2011). Positioning of Single Co Atoms Steered by a Self-Assembled Organic Molecular Template. *J. Phys. Chem. Lett.* **2**, 1639–1645.
[102] Pivetta, M., Pacchioni, G.E., Schlickum, U., Barth, J.V., Brune, H. (2013). Formation of Fe Cluster Superlattice in a Metal-Organic Quantum-Box Network. *Phys. Rev. Lett.* **110**, 086102.
[103] Zhang, R., Lyu, G., Chen, C., Lin, T., Liu, J., Liu, P.N., Lin, N. (2015). Two-Dimensional Superlattices of Bi Nanoclusters Formed on a Au(111) Surface Using Porous Supramolecular Templates. *ACS Nano* **9**, 8547–8553.
[104] Gragnaniello, L., Paschke, F., Erler, P., Schmitt, P., Barth, N., Simon, S., Brune, H., Rusponi, S., Fonin, M. (2017). Uniaxial 2D Superlattice of Fe_4 Molecular Magnets on Graphene. *Nano Lett.* **17**, 7177–7182.
[105] Degen, S.; Krupski, A.; Kralj, M.; Langner, A.; Becker, C.; Sokolowski, M. and Wandelt, K. (2005) Determination of the coincidence lattice of an ultrathin Al_2O_3 film on $Ni_3Al(111)$, *Surf. Sci.*, **576**, L57-L70.
[106] Néel, N.; Kröger, J. and Berndt, R. (2006) Highly Periodic Fullerene Nanomesh, *Adv. Mat.*, **18**, 174-177.
[107] Didiot, C.; Pons, S.; Kierren, B.; Fagot-Revurat; Y. and Malterre, D. (2007) Nanopatterning the electronic properties of gold surfaces with self-organized superlattices of metallic nanostructures, *Nature Nanotech.*, **2**, 617-621.
[108] Rohart, S.; Girard, Y.; Nahas, Y.; Repain, V.; Rodary, G.; Tejeda, A. and Rousset, S. (2008) Growth of iron on gold (7 8 8) vicinal surface: From nanodots to step flow. *Surf. Sci.*, **602**, 28-36.
[109] Brune, H.; Giovannini, M.; Bromann, K. and Kern K. (1998) Self-organized growth of nanostructure arrays on strain-relief patterns. *Nature*, **394**, 451-453.
[110] Rohart, S.; Baudot, G.; Repain, V.; Girard, Y.; Rousset, S.; Bulou, H.; Goyhenex, and C., Proville, L. (2004) Atomistic mechanisms for the ordered growth of Co nanodots on Au(7 8 8): a comparison between VT-STM experiments and multi-scaled calculations. *Surf. Sci.*, **559**, 47-62.
[111] Repain, V.; Rohart, S.; Girard, Y.; Tejeda, A. and Rousset, S. (2006) Building uniform and long-range ordered nanostructures on a surface by nucleation on a point defect array. *J. Phys.: Condens. Matter*, **18**, S17-S26.
[112] Boishin, G.; Sun, L.D.; Hohage, M., and Zeppenfeld, P. (2002) Growth of cobalt on the nanostructured Cu–CuO(110) surface. *Surf. Sci.*, **512**, 195-200.

[113] Nahas, Y.; Repain, V.; Chacon, C.; Girard, Y. and Rousset, S. (2010) Interplay between ordered growth and intermixing of Pt on patterned Au surfaces. *Surf. Sci.*, **604**, 829-833.
[114] Venables, J. (2000) *Introduction to Surface and Thin Film Processes.* Cambridge University Press, Cambridge.
[115] Brune, H.; Bales, G.S.; Jacobsen, J.; Boragno, C. and Kern, K. (1999) Measuring surface diffusion from nucleation island densities. *Phys. Rev. B*, **60**, 5991-6006.
[116] Amar, J.G., and Family, F. (1995) Critical Cluster Size: Island Morphology and Size Distribution in Submonolayer Epitaxial Growth. *Phys. Rev. Lett.*, **74**, 2066-2079.
[117] Venables, J. (1997) Nucleation growth and pattern formation in heteroepitaxy. *Phys. A*, **239**, 35.
[118] Bulou, H., Scheurer, F., Goyhenex, C., Speisser, V., Romeo, M., Carrière, B., Moreau, N., Repain, V., Chacon, C., Girard, Y., Lagoute, J., Rousset, S., Otero, E., Ohresser, P. (2013). Thermodynamics versus kinetics in a morphology transition of nanoparticles. *Phys. Rev. B* **87**, 155404.
[119] Nahas, Y.; Repain, V.; Chacon, C.; Girard, Y.; Lagoute, J.; Rodary, G.; Klein, J.; Rousset, S.; Bulou, H. and Goyhenex, C. (2009) Dominant Role of the Epitaxial Strain in the Magnetism of Core-Shell Co/Au Self-Organized Nanodots, *Phys. Rev. Lett.*, **103**, 067202.
[120] Campiglio, P., Moreau, N., Repain, V., Chacon, C., Girard, Y., Klein, J., Lagoute, J., Rousset, S., Bulou, H., Scheurer, F., Goyhenex, C., Ohresser, P., Fonda, E., Magnan, H. (2011). Interplay between interfacial and structural properties on the magnetism of self-organized core-shell Co/Pt supported nanodots. *Phys. Rev. B* **84**, 235443.
[121] Bott, M.; Hohage, M.; Morgenstern, M.,; Michely, T. and Comsa, G. (1996) New Approach for Determination of Diffusion Parameters of Adatoms, *Phys. Rev. Lett.*, **76**, 1304-1307.
[122] Kyuno, K.; Gölzhäuser, A. and Ehrlich, G. (1998) Growth and the diffusion of platinum atoms and dimers on Pt(111), *Surf. Sci.*, **397**, 191-196.
[123] Michely, T.; Hohage, M.; Bott, M. and Comsa, G. (1993) Inversion of Growth Speed Anisotropy in Two Dimensions, *Phys. Rev. Lett.*, **70**, 3943-3946.
[124] Bromann, K.; Brune, H.; Röder, H. and Kern, K. (1995) Interlayer mass transport in homo- and heteroepitaxial metal growth, *Phys. Rev. Lett.*, **75**, 677-679.
[125] Rottler, J. and Maass, P. (1999) Second Layer Nucleation in Thin Film Growth, *Phys. Rev. Lett.*, **83**, 3490-3493.
[126] Heinrichs, S.; Rottler, J. and Maass, P. (2000) Nucleation on top of islands in epitaxial growth, *Phys. Rev. B*, **62**, 8338-8359.
[127] Weiss, N. (2004) Propriétés Magnétiques de Nanostructures de Cobalt Adsorbées, Swiss Federal Institute of Technology, Lausanne.
[128] Röder, H.; Bromann, K.; Brune, H. and Kern, K. (1997) Strain mediated two-dimensional growth kinetics in metal heteroepitaxy: Ag/Pt(111), *Surf. Sci.*, **376**, 13-31.

[129] Rusponi, S.; Cren, T.; Weiss, N.; Epple, M.; Buluschek, P.; Claude, L. and Brune, H. (2003) The remarkable difference between surface and step atoms in the magnetic anisotropy of 2D nanostructures, *Nat. Mater.*, **2**, 546-551.
[130] Ouazi, S.; Vlaic, S.; Rusponi, S.; Moulas, G.; Buluschek, P.; Halleux, K.; Bornemann, S.; Mankovsky, S.; Minar, J.; Staunton, J. B.; Ebert, H. and Brune, H. (2012) Atomic Scale Engineering of Magnetic Anisotropy of Nanostructures through Interfaces and Interlines, *Nat. Communic.* **3**, 1313.
[131] Moreau, N., Repain, V., Chacon, C., Girard, Y., Lagoute, J., Klein, J., Rousset, S., Scheurer, F., Ohresser, P. (2014). Growth and magnetism of self-organized Co_xPt_{1-x} nanostructures on Au(111). *J. Phys. D: Appl. Phys.* **47**, 075306.
[132] Pivetta, M., Rusponi, S., Brune, H. (2018). Direct capture and electrostatic repulsion in the self-assembly of rare-earth atom superlattices on graphene. *Phys. Rev. B* **98**, 115417.
[133] Baltic, R., Pivetta, M., Donati, F., Wäckerlin, C., Singha, A., Dreiser, J., Rusponi, S., Brune, H. (2016). Superlattice of Single Atom Magnets on Graphene. *Nano Lett.* **16**, 7610–7615.
[134] Brandstetter, T., Wagner, T., Fritz, D.R., Zeppenfeld, P. (2010). Tunable Ag Nanowires Grown on Cu(110)-Based Templates. *J. Phys. Chem. Lett.* **1**, 1026–1029.
[135] Sahaf, H., Léandri, C., Moyen, E., Macé, M., Masson, L., Hanbücken, M. (2009). Growth of Co nanolines on self-assembled Si nanostripes. *EPL* **86**, 28006.
[136] Gambardella, P., Blanc, M., Bürgi, L., Kuhnke, K., Kern, K. (2000). Co growth on Pt(997): from monatomic chains to monolayer completion. *Surface Science* **449**, 93–103.
[137] Gambardella, P., Blanc, M., Kuhnke, K., Kern, K., Picaud, F., Ramseyer, C., Girardet, C., Barreteau, C., Spanjaard, D., Desjonquères, M.C. (2001). Growth of composition-modulated Ag/Co wires on Pt(997). *Phys. Rev. B* **64**, 045404.
[138] Garel, M., Babonneau, D., Boulle, A., Pailloux, F., Coati, A., Garreau, Y., Y. Ramos, A., N. Tolentino, H.C. (2015). Self-organized ultrathin FePt nanowires produced by glancing-angle ion-beam codeposition on rippled alumina surfaces. *Nanoscale* **7**, 1437–1445.
[139] Yazidi, S., Fafin, A., Rousselet, S., Pailloux, F., Camelio, S., Babonneau, D. (2015). Structure and far-field optical properties of self-organized bimetallic Au_x-Ag_{1-x} nanoparticles embedded in alumina thin films. *physica status solidi c* **12**, 1344–1348.
[140] Fafin, A., Yazidi, S., Camelio, S., Babonneau, D. (2016). Near-Field Optical Properties of Ag_xAu_{1-x}Nanoparticle Chains Embedded in a Dielectric Matrix. *Plasmonics* **11**, 1407–1416.
[141] Fruchart, O., Klaua, M., Barthel, J., Kirschner, J., 1999. Self-Organized Growth of Nanosized Vertical Magnetic Co Pillars on Au(111). *Phys. Rev. Lett.* **83**, 2769–2772.
[142] Schuler, V., Milano, J., Coati, A., Vlad, A., Sauvage-Simkin, M., Garreau, Y., Demaille, D., Hidki, S., Novikova, A., Fonda, E., Zheng, Y., Vidal, F. (2016). Growth and magnetic properties of vertically aligned epitaxial CoNi nanowires in (Sr, Ba)TiO_3 with diameters in the 1.8–6 nm range. *Nanotechnology* **27**, 495601.

[143] Hennes, M., Schuler, V., Weng, X., Buchwald, J., Demaille, D., Zheng, Y., Vidal, F. (2018). Growth of vertically aligned nanowires in metal–oxide nanocomposites: kinetic Monte-Carlo modeling versus experiments. *Nanoscale* **10**, 7666–7675.
[144] Hennes, M., Weng, X., Fonda, E., Gallas, B., Patriarche, G., Demaille, D., Zheng, Y., Vidal, F. (2019). Phase separation and surface segregation in Co-Au-$SrTiO_3$ thin films: Self-assembly of bilayered epitaxial nanocolumnar composites. *Phys. Rev. Materials* **3**, 035002.
[145] Bonilla, F.J., Novikova, A., Vidal, F., Zheng, Y., Fonda, E., Demaille, D., Schuler, V., Coati, A., Vlad, A., Garreau, Y., Sauvage Simkin, M., Dumont, Y., Hidki, S., Etgens, V. (2013). Combinatorial Growth and Anisotropy Control of Self-Assembled Epitaxial Ultrathin Alloy Nanowires. *ACS Nano* **7**, 4022–4029.
[146] Kim, D.H., Sun, X.Y., Aimon, N.M., Kim, J.J., Campion, M.J., Tuller, H.L., Kornblum, L., Walker, F.J., Ahn, C.H., Ross, C.A. (2015). A Three Component Self-Assembled Epitaxial Nanocomposite Thin Film. *Advanced Functional Materials* **25**, 3091–3100.
[147] Dietz, T.G.; Duncan, M.A.; Powers, D.E.; Smalley, R.E. (1981), Laser production of supersonic metal cluster beams *The Journal of Chemical Physics,* **74**, 6511-6512.
[148] Bardotti, L.; Tournus, F.; Pellarin, M.; Broyer, M.; Mélinon, P. and Dupuis, V. (2012) Spontaneous formation of size-selected bimetallic nanoparticle arrays. *Surf. Sci.*, **606**, 110-114.
[149] Bardotti, L.; Tournus, F.; Mélinon, P.; Pellarin, M. and Broyer, M. (2011) Mass-selected clusters deposited on graphite: Spontaneous organization controlled by cluster surface reaction. *Phys. Rev. B*, **83**, 035425.
[150] Tournus, F.; Bardotti, L. and Dupuis V. (2011) Size-dependent morphology of CoPt cluster films on graphite: A route to self-organization. *J. of Appl. Phys.*, **109**, 114309.
[151] Weaver, J. H. and Waddill, G. D. (1991) Cluster Assembly of Interfaces: Nanoscale engeneering, *Science*, **251**, 1444-1451
[152] Bromann, K.; Brune, H.; Félix, C.; Harbich, W.; Monot, R.; Buttet, J., and Kern, K. (1997) Hard and soft landing of mass selected Ag clusters on Pt(111), *Surf. Sci.*, **377-379**, 1051-1055.
[153] Brihuega, I.; Michaelis, C. H.; Zhang, J.; Bose, S.; Sessi, V.; Honolka, J.; Schneider, M. A.; Enders, A. and Kern, K. (2008) Electronic decoupling and templating of Co nanocluster arrays on the boron nitride nanomesh, *Surf. Sci.*, **602**, L95-L99.
[154] Zhang, J.; Sessi, V.; Michaelis, C. H., Brihuega, I.; Honolka, J.; Kern, K.; Skomski, R.; Chen, X.; Rojas, G. and Enders, A. (2008) Ordered layers of Co clusters on BN template layers, *Phys. Rev. B*, **78**, 165430.
[155] Natterer, F. D.; Patthey, F.; and Brune, H. (2012) Ring State for Single Transition Metal Atoms on Boron Nitride on Rh(111), *Phys. Rev. Lett.*, **109**, 066101.
[156] Huang, L.; Chey, S. J. and Weaver, J. H. (1998) Buffer-Layer-Assisted Growth of Nanocrystals: Ag-Xe-Si(111), *Phys. Rev. Lett.*, **80**, 4095-4098.
[157] Haley, C. and Weaver, J. H. (2002) Buffer-layer-assisted nanostructure growth via two-dimensional cluster–cluster aggregation, *Surf. Sci.*, **518**, 243-250.

[158] Antonov, V. N.; Palmer, J. S.; Waggoner, P. S.; Bhatti, A. S. and Weaver, J. H. (2004) Nanoparticle diffusion on desorbing solids: The role of elementary excitations in buffer-layer-assisted growth, *Phys. Rev. B*, **70**, 045406.
[159] Pierce, J. P.; Torija, M. A.; Gai, Z.; Shi, J.; Schulthess, T. C.; Farnan, G. A.; Wendelken, J. F.; Plummer, E. W. and Shen, J. (2004) Ferromagnetic Stability in Fe Nanodot Assemblies on Cu(111) Induced by Indirect Coupling through the Substrate, *Phys. Rev. Lett.*, **92**, 237201.
[160] Palmer, J. S.; Swaminathan, P.; Babar, S. and Weaver, J. H. (2008) Solid-state dewetting-mediated aggregation of nanoparticles, *Phys. Rev. B*, **77**, 195422.
[161] Kosiorek, A.; Kandulski, W.; Glaczynska, H. and Giersig, M. (2005) Fabrication of Nanoscale Rings, Dots, and Rods by Combining Shadow Nanosphere Lithography and Annealed Polystyrene Nanosphere Masks, *Small*, **1**, 439-444.
[162] Chen, J.; Liao, W. S.; Chen, X.; Yang, T.; Wark, S. E.; Son, D. H.; Batteas, J. D. and Cremer, P. S. (2009). Evaporation-Induced Assembly of Quantum Dots into Nanorings, *ACS Nano*, **3**, 173-180.